Early detection of forest stress from European spruce bark beetle attack, and a new vegetation index: Normalized distance red & SWIR (NDRS)

Langning Huo [*], Henrik Jan Persson, Eva Lindberg

Department of Forest Resource Management, Swedish University of Agriculture Sciences, SE-901 83 Umeå, Sweden

ARTICLE INFO

ABSTRACT

The European spruce bark beetle (*Ips typographus* [L.]) is one of the most damaging pest insects of European spruce forests. A crucial measure in pest control is the removal of infested trees before the beetles leave the bark, which generally happens before the end of June. However, stressed tree crowns do not show any significant color changes in the visible spectrum at this early-stage of infestation, making early detection difficult. In order to detect the related forest stress at an early stage, we investigated the differences in radar and spectral signals of healthy and stressed trees. How the characteristics of stressed trees changed over time was analyzed for the whole vegetation season, which covered the period before attacks (April), early-stage infestation ('green-attacks', May to July), and middle to late-stage infestation (August to October). The results show that spectral differences already existed at the beginning of the vegetation season, before the attacks. The spectral separability between the healthy and infested samples did not change significantly during the 'green-attack' stage. The results indicate that the trees were stressed before the attacks and had spectral signatures that differed from healthy ones. These stress-induced spectral changes could be more efficient indicators of early infestations than the 'green-attack' symptoms.

In this study we used Sentinel-1 and 2 images of a test site in southern Sweden from April to October in 2018 and 2019. The red and SWIR bands from Sentinel-2 showed the highest separability of healthy and stressed samples. The backscatter from Sentinel-1 and additional bands from Sentinel-2 contributed only slightly in the Random Forest classification models. We therefore propose the Normalized Distance Red & SWIR (NDRS) index as a new index based on our observations and the linear relationship between the red and SWIR bands. This index identified stressed forest with accuracies from 0.80 to 0.88 before the attacks, from 0.80 to 0.82 in the early-stage infestation, and from 0.81 to 0.91 in middle- and late-stage infestations. These accuracies are higher than those attained by established vegetation indices aimed at 'green-attack' detection, such as the Normalized Difference Water Index, Ratio Drought Index, and Disease Stress Water Index. By using the proposed method, we highlight the potential of using NDRS with Sentinel-2 images to estimate forest vulnerability to European spruce bark beetle attacks early in the vegetation season.

1. Introduction

During the last 50 years, the European spruce bark beetle (*Ips typographus* [L.]) has killed more than 150 million m³ forest in Europe (Schroeder and Cocoş, 2018), where it is the most economically destructive insect pest of coniferous forests in Europe (Biedermann et al., 2019). With the aggravation of global warming, several studies (Jakoby et al., 2019; Potterf et al., 2019) have predicted additional bark beetle generations, earlier spring swarming, more aggravated swarming, and more drought and storm events. These trends have been verified by

the outburst of bark beetles in Sweden, which is located further north than the central European countries where bark beetle attacks first occurred. Spruce bark beetles cause most damage to spruce (*Picea abies*) forest in southern Sweden. In 2018, it destroyed 3–4 million m³ forest, causing losses valued at several hundreds of millions of Euros. With the extremely warm summer of 2018, an additional generation of bark beetles occurred in August, increasing the amount of attacked Swedish forest to 7 million m³ in 2019. Such destruction of forest causes not only economic losses but also forms a serious threat to the forest ecosystem (Huang et al., 2019).

One crucial strategy to control bark beetles is to identify and remove attacked trees while larvae are still inside the stems. The most difficult aspect for forest management is that reduced vitality is not visible in the tree crowns at the early stage of an infestation when the lack of any color change makes the detection of attack difficult. However, remote sensing can acquire data at wavelengths beyond the visual spectrum and potentially map changes caused by bark beetles. The earliest that bark beetle attacks can be detected by remote sensing is a crucial factor that has been studied in different regions. Both pine bark beetle attacks in North America and spruce bark beetle attacks in Europe are commonly divided into three stages of infestation according to the difficulty of sensing in the visible spectra: (1) 'green-attack', a period with no abnormal visible colors in the tree crowns during bark beetle colonization; (2) 'red-attack', a period when the crowns turn yellow or reddish with significantly decreased water content in the needles; (3) 'gray-attack', when coniferous trees gradually lose needles after dying.

Detection of tree mortality and 'green-attacks' of mountain pine beetles have been conducted since the 1960s to date (Puritch, 1981; Tane et al., 2018; Wulder et al., 2006), using remote sensing data including Landsat imagery (Coops et al., 2006b; Meddens et al., 2013), QuickBird (Coops et al., 2006a), Hyperion data (White et al., 2007), aerial images (Meddens et al., 2011), and lidar data (Coops et al., 2009). The results have generally illustrated that the detection rate at the red and gray stage was high, but the detection of 'green-attacks' was poor, despite water stress at the leaf-level clearly being detectable at this stage (Puritch, 1981; Wulder et al., 2006; Wulder et al., 2009). Similar results

from studies on European spruce bark beetles have also reported low accuracy of identifying 'green-attacks' (Abdullah et al., 2019b; Immitzer and Atzberger, 2014; Klouček et al., 2019). Recent studies covering 'green-attacks' (Table 1) have investigated the detection of spruce bark beetle attacks using data from currently available sensors, e.g., Sentinel-2, TerraSAR-X, airborne laser scanning (ALS), and terrestrial laser scanning (TLS). The studies listed in Table 1 (including our study) have all focused on the European spruce bark beetle (*Ips typographus* [L.]) and do not include other species with different life cycles.

Reviewing the studies in Table 1, we found that the timing of 'green-attacks' varies among individual trees, and depends both on when the trees first come under attack and the climate zone. For example, Abdullah et al. (2019c) observed 'green-attacks' from 15 May to 1 June by field inventory and considered 'green-attacks' within 15–30 days after the early stage of infestation. Klouček et al. (2019) considered 15 June as the beginning of the outbreak and showed 'green-attacks' on 1 August and 'yellow-attack' on 30 August. Junttila et al. (2019) inventoried 'green-attacked' trees in August, and classified them into low and moderate infestations according to the symptoms. Näsi et al. (2015) conducted a field inventory in August and found yellowish and reddish trees under infestation. Based on the evidence from these studies, 'green-attacks' by first generation beetles usually appear from May to July, while August seems to be the transition from green to yellow stages.

However, 'green-attack' cannot always be detected early enough to allow forest pest control and damage management to be implemented. In general, for central and northern Europe, the bark beetles emerge

Table 1

Overview of studies of spruce bark beetle attack detection, from the scale of needle to pixel and plot scale.

Location of study area	Platform/Sensor	Available bands/ wavelength	Used/important bands	Year	Month	'Green-attacks detection	Scale	Reference
Southeast Germany	Spectrometer	350–2500 nm	Visible, NIR, SWIR	2015	Early summer	✓	Needles	Abdullah et al. (2018)
Lahti, Finland	UAV camera	500–900 nm	Vegetation indices	2013	Late August	–	Individual tree	Näsi et al. (2015)
Czech	UAV camera	Red, green, blue, NIR	Green, red	2017	Middle June Early August Late August Early October	✓	Individual tree	Klouček et al. (2019)
Polish-Belarusian border	ALS and color-infrared (CIR) imagery	Point cloud heights	Change of the point cloud heights, NDVI, green	2015	Early July (leaf-on) November and December (leaf-off)	–	Individual tree	Kamińska et al. (2018)
Southeast Finland	TLS	1550 nm 905 nm	Intensity metrics	2017	August	✓	Individual tree	Junttila et al. (2019)
Central Austria	Worldview-2	RGB, red-edge, NIR	Red and yellow	2010	Middle June	✓	2 m pixels	Immitzer and Atzberger (2014)
Southeast Germany	Aircraft hyperspectral camera	450–2480 nm	Wavelength 455, 528, 690 nm	2009	Late August	–	4 m pixels 7 m pixels	Lausch et al. (2013)
Southeast Germany	Airborne hyperspectral camera	125 channels from 450 to 2480 nm	Green, red-edge, SWIR	2009	Late August	–	7 and 5 m pixels	Fassnacht et al. (2014)
Biberach, Germany	RapidEye TerraSAR	410–850 nm Backscattering coefficient	NDVI, backscattering coefficient	2009	Late May	✓	10 m pixels	Ortiz et al. (2013)
Southern Sweden	Sentinel-2	492–2202 nm	Water content related VIs (DWSI, MSI, NDWI, VMI)	2018	Early July Late July Late October	✓	20 m pixels	Yang (2019)
Southeast Germany	SPOT-2 SPOT-4 Landsat-7	Green, red, NIR Green, red, NIR, SWIR Blue, green, NIR, SWIR	Red, NIR, Green Red, SWIR, NIR, green NIR, red, SWIR	2001–2011	August to October	–	20 m pixels 20 m pixels 30 m pixels	Latifi et al. (2014)
Southeast Germany	Sentinel-2 Landsat-8	492–2202 nm 430–2290 nm	SWIR, NIR, red	2016	Early June	✓	30 m × 30 m plots	Abdullah et al. (2019b)
Southeast Germany	Landsat-8	430–2290 nm	Canopy surface temperature	2016	May, July, August	✓	30 m × 30 m plots	Abdullah et al. (2019a)
Southeast Germany	TapidEye SPOT-5 Airborne camera	440–850 nm 480–1750 nm Red, green, NIR	Red-edge, NIR	2015	Middle May Early June Early July	✓	Plots	Abdullah et al. (2019c)

from pupae as adults and leave the bark as early as the end of June (Abdullah, 2019; Yang, 2019), although this timing is also related to the air temperature (Wermelinger, 2004). The goal of most studies has therefore been the early detection of attacks in May and June, so that infested trees can be removed together with the larvae and pupae they contain. Moreover, for large areas of forest, even earlier detection helps forest managers to plan and conduct the sanitation cutting in good time.

When drawing conclusions from previous studies concerning the early detection of forest stress from spectral images, there are still several areas of uncertainty. First, studies have focused on the spectral characteristics when the 'green-attack' had been going on for at least half a month, but few have presented the spectral characteristics from the beginning or even before the start of an attack. Most studies in Table 1 detected spectral responses to attacks from the earliest image available, which does not exclude the possibility of detecting stressed forest before the infestation. Most studies regarded May and June as the early stage of attacks and considered any spectral differences at this period to be evidence of detecting 'green-attack'; but they did not consider the possibility that such differences may have existed before the attacks. This hypothesis cannot be excluded, especially considering that bark beetles preferentially attack weaker trees with a lower ability to launch their defense mechanisms (Wermelinger, 2004), and that weak and healthy forests might have different spectral features. Therefore, studies should be conducted by extending the time range of the spectral signatures, including images before and at the beginning of attacks. This would enable an improved analysis of how the spectral signatures are influenced during the 'green-attack' stage.

Second, sensors on different platforms, e.g. laboratory, UAV, and satellites, have given rise to different spectral responses to the infestation. For example, Abdullah et al. (2018) reported a significant decrease in reflectance in the near infrared (NIR) bands after infestation in a laboratory environment, while Ortiz et al. (2013) observed increasing NIR pixel values from RapidEye images. With larger pixels, more of the surroundings are included in the pixels, diluting any subtle changes caused by bark beetle attacks, especially at an early stage. The use of satellite images to achieve early detection should therefore be studied further, although clear changes in spectrometer measurements of needles have been observed (Abdullah et al., 2018; Foster et al., 2017).

Third, alternative vegetation indices should be explored for their ability to detect stress without using the NIR and red-edge bands, which have shown inconsistent trends in different studies, as mentioned above. This influences the efficiency of commonly used NIR-based indices like the Normalized Difference Vegetation Index (NDVI) and the Normalized Difference Water Index (NDWI), even though they have been used and recommended in bark beetle attack identification. For example, Klouček et al. (2019) concluded that the performance of the indices based on the NIR band was even lower than the single red band. The visible and short wave infra red (SWIR) bands have shown similar responses in different studies and appear to be less influenced by the observation scales (Abdullah et al., 2018; Klouček et al., 2019; Minařík and Langhammer, 2016; Näsi et al., 2015). The combinations of visible and SWIR bands therefore have the potential to improve attack detection.

In addition to optical images, radar data have recently been investigated for their ability to reveal insect damage in forests (Hollaus and Vreugdenhil, 2019). The backscatter σ^o derived from C-band radar data has been shown to be sensitive to vegetation structure (Dostálová et al., 2018; Frison et al., 2018; Veloso et al., 2017) and moisture content (Paloscia et al., 2013; Veloso et al., 2017; Wang et al., 1998), both of which can be indicators of forest damage. Studies have been conducted to illustrate whether damage caused by forest insects could induce significant changes in the radar signal. To date, five studies have detected forest insect damage; four detecting defoliation and tree mortality (Kaasalainen et al., 2010; Ranson et al., 2003; Tanase et al., 2018; Xue and Su, 2017; Xue et al., 2018), and only one focusing on early-stage detection (Ortiz et al., 2013). Among these five studies, only Tanase et al. (2018) reported a significant decrease in σ^o that can be used as a

threshold to classify attacks from the L-band ALOS PALSAR images, while Ortiz et al. (2013) and Xue et al. (2018) illustrated the contribution of X-band and C-band radar images in non-parametric models for detecting attacked trees.

This study investigated how forest stress could be detected using satellite data. The study had three objectives: (1) To investigate the differences in the radar and spectral signals of healthy and stressed trees throughout the whole vegetation season; (2) To investigate the potential of detecting stress early, i.e. before and during the 'green-attacks'; (3) To develop methods of identifying forest stress related to bark beetle attacks.

2. Materials

We used two reference datasets in our study: Dataset-2019, comprising 78 plots with 15 m radii inventoried in the field during 2019; and Dataset-2018, comprising 200 locations derived from visual interpretation of high-resolution satellite images (Pleiades) from 2018. Throughout the entire study, the signal analyses and development of methods were conducted on the satellite images from Sentinel-1 and 2 using Dataset-2018, and the proposed detection methods were validated using Dataset-2019.

2.1. Study area

The study area located at Remningstorp, Västra Götaland, Sweden (58°27′18″N, 13°39′8″E) covers an area of 1602 ha. The forests in this area are mainly spruce (*Picea abies*) and pine (*Pinus sylvestris*) managed for wood production. According to the swarm monitoring station at Nässjö, around 160 km southeast of the study area, the bark beetles started swarming and attacking trees in the week from April 16 to 22, 2018, and April 15 to 21, 2019. Both years experienced attacks from two bark beetle generations. The offspring of the first generation increased the swarming from late July to early August. Most of the offspring from the second generation remained in the bark at least until early September.

2.2. Satellite data and pre-processing

Satellite images from Sentinel-1 and 2 were used to detect forest stress due to bark beetle attacks, while images from Pleiades were interpreted visually to obtain reference data in 2018 (Fig. 1).

Radar images were obtained from the Sentinel-1 satellites, which are currently comprised of a constellation of two polar-orbiting satellites, each with a C-band synthetic aperture radar (SAR). From Sentinel-1A and 1B, Level-1 Ground Range Detected (GRD) radar products in the Interferometric Wide (IW) swath mode were acquired from a descending orbit every 6 days from March 2018 to November 2019. The IW mode provides data in VV and VH dual polarization, and the GRD products are provided as pixels with size 10 m × 10 m. The radar data were pre-processed with SNAP (ESA Sentinel Application Platform v7.0 http://step.esa.int). The pre-processing to derive the backscatter σ^o included precise orbit correction, radiometric calibration and orthorectification supported by an external LiDAR-based DTM. All images were co-registered to a stack and histogram-matched to the S1 image from 3 July 2018, which was used as reference, to suppress variations due to weather effects. Finally, multi-temporal speckle filtering was conducted with a moving window of seven images along the time domain, and hence no spatial averaging was carried out in order to preserve the spatial resolution.

Optical images were obtained from Sentinel-2 and Pleiades, where the Sentinel-2 images were used for the experimental study and the Pleiades images as high-resolution reference. Cloud-free Sentinel-2A and 2B L2A images were acquired from Copernicus Open Access Hub over the study area from March 2018 to November 2019. The L2A products giving the bottom of atmosphere reflectance (12-bit, [0, 4095])
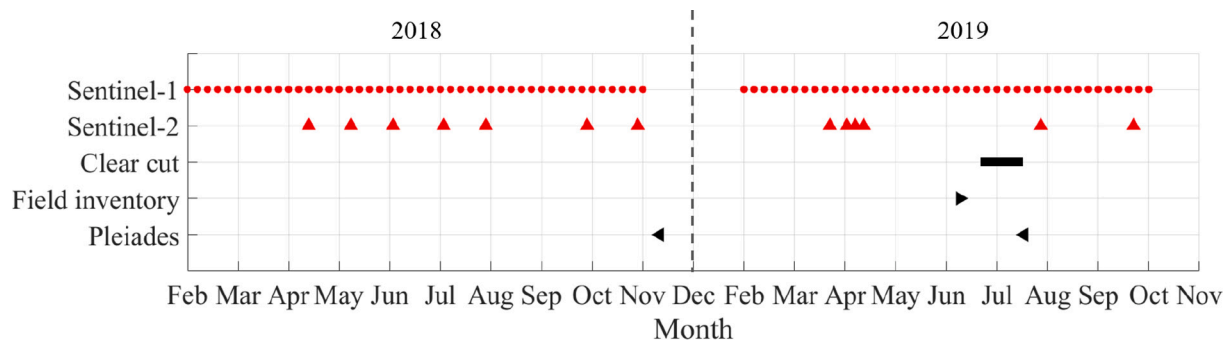
Fig. 1. Timeline of the datasets used in the present study.

were provided by ESA. The spectral and spatial resolutions are presented in Table 2. The spectral bands acquired with Sentinel-2 have 10 m to 60 m resolution. However, the Bands 1, 9 and 10, with 60 m resolution, were excluded due to their pixel size compared to the much smaller plot sizes. The bands with 20 m resolution (Bands 5, 6, 7, 8A, 11 and 12) were resampled to 10 m resolution to match the Bands 2, 3, 4, and 8 from Sentinel-2 and the backscatter σ^o from Sentinel-1. No histogram matching was performed when presenting the difference between healthy and stressed pixels in the raw bands and vegetation indices, since it would remove the seasonal effects.

Because the available Sentinel-2 images from 2019 were limited, our study mainly used the dataset from 2018 for the analyses, and the results were validated against the 2019 dataset.

The two Pleiades images were acquired on 6 November 2018 and 17 July 2019, and were visually interpreted to obtain the reference data as described in the next section. The images were delivered as pan-sharpened along-track stereo triplets in four bands (blue, green, red, near infrared), with a spatial resolution of 0.5 m and with a primary processing level, which contains corrections for radiometric and sensor distortions, using internal calibration parameters, ephemeris, and attitude measurements. The blue band wavelength was 495 nm (central, bandwidth 430–560 nm), green 559 nm (500–617 nm), red 656 nm (590–722 nm), and near-infrared 843 nm (740–945 nm). Only the nadir image was used for the visual interpretation.

2.3. Reference data

2.3.1. Field inventory

A field inventory was conducted in June 2019 (Dataset-2019). The presence of bark beetle attack was identified by visual inspection of stripped bark, entrance holes, resin flows, frass and traces of wood-peckers having searched for the insects. When attacked trees were found, a sample plot center was defined at the middle of the attacked area to include as many affected trees as possible. If no on-going spruce

bark beetle attacks were found in a stand, a healthy sample plot was placed entirely within the homogeneous stand.

In total 78 sample plots with 15 m radius were inventoried and the locations registered with DGPS coordinates. These included 38 plots with on-going bark beetle attacks and 40 healthy plots. Trees suffering attack, other damage, and dead trees were counted and recorded. In plots with attacked trees, the proportion actually subject to bark beetle attack ranged from 18% to 60%, with 30% as the average (Fig. 2).

2.3.2. Visual interpretation

A 2017 stand delineation map made by a professional photo interpreter was used to select the spruce dominated stands. Spruce stands (defined in blue in Fig. 1) were selected as those with >80% spruce volume and age > 30 years. In total, 238 stands were used after removing areas that were clear-cut in the period 2018 to 2019.
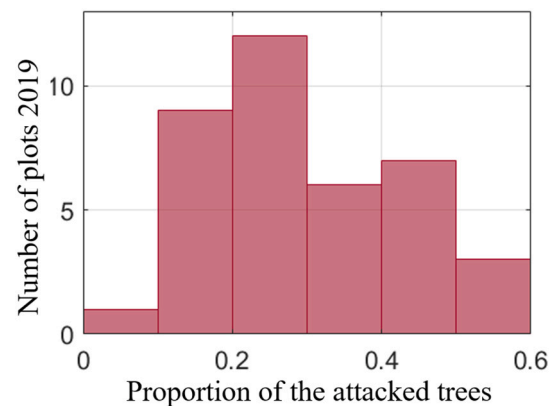
Fig. 2. Number of plots with different proportions of attacked trees.

Table 2
Wavelength and spatial resolution of Sentinel-2 images.

Sentinel-2 bands	Sentinel-2A		Sentinel-2B		Spatial resolution (m)
	Central wavelength (nm)	Bandwidth (nm)	Central wavelength (nm)	Bandwidth (nm)	
Band 1 – Coastal aerosol	442.7	21	442.2	21	60
Band 2 – Blue	492.4	66	492.1	66	10
Band 3 – Green	559.8	36	559.0	36	10
Band 4 – Red	664.6	31	664.9	31	10
Band 5 – Vegetation red-edge	704.1	15	703.8	16	20
Band 6 – Vegetation red-edge	740.5	15	739.1	15	20
Band 7 – Vegetation red-edge	782.8	20	779.7	20	20
Band 8 – NIR	832.8	106	832.9	106	10
Band 8A – Narrow NIR	864.7	21	864.0	22	20
Band 9 – Water vapor	945.1	20	943.2	21	60
Band 10 – SWIR – Cirrus	1373.5	31	1376.9	30	60
Band 11 – SWIR	1613.7	91	1610.4	94	20
Band 12 – SWIR	2202.4	175	2185.7	185	20

Two maps, marked with the approximate locations of attacked trees as recorded in 2018 and 2019, were obtained from the local forest managers. To obtain the precise positions of the attacks, visual interpretation was conducted using a Pleiades image from 6 November 2018. At the recorded locations, the attacked tree crowns were visible as gray when visualizing the image in red-green-blue (R-G-B) mode, and visible as green in IR-red-blue (IR-R-B) mode (Fig. 3). Healthy trees appeared in green and red in R-G-B and IR-R-B mode, respectively. One Pleiades image from 17 July 2019 was then used to avoid selecting deciduous trees, which show up in a similar color to that of attacked trees in winter, but are better differentiated in summer.

In total, 100 healthy and 100 attacked locations were interpreted. 10 m pixels were obtained from the Sentinel images covering the 200 locations and used as the samples of Dataset-2018. In the following sections, pixels covering the healthy trees are denoted healthy pixels, and pixels covering the attacked trees are denoted stressed pixels.

To summarize, we had 200 interpreted pixels in Dataset-2018 and 78 field-inventoried plots in Dataset-2019. Their locations were independently selected (Fig. 4). The healthy and attacked samples had similar biomass distributions (Fig. 5), with an average of 234 and 233 t∕ha respectively for 2018, and 223 and 255 t∕ha for 2019. We took the biomass into consideration since it affects the spectral and radar signal (Chen et al., 2019; Navarro et al., 2019; Saatchi et al., 2011). The reference biomass map was generated using 10 m field plots and airborne laser scanning data within a previous biomass project (Persson and Fransson, 2014; Soja et al., 2015), where a wall-to-wall map of the biomass was derived from ALS data with reference data for the biomass estimated using established functions with the diameter at breast height (DBH) and height measured in field plots as descriptive variables.

3. Methods

The present study includes four sections, with results from the former sections providing inputs to the design of the later sections (Fig. 6). In section 3.1, we compared the radar and optical signals between healthy and stressed pixels. It gave us a first impression of the information content of each data source, e.g., illustrating signal changes due to the infestation stages or seasonal effects. The figures guided us in the subsequent procedures in which vegetation indices were defined and tested. The classification in section 3.1 is a quantitative description of the separability of each band using linear discriminant analysis (LDA). In the second Section (3.2), we used 12 vegetation indices to quantify the separability of the healthy and stressed pixels. The third Section (3.3) describes a non-parametric classification using all the bands and optimized combinations of the bands. The importance of different bands derived in this section provided a crucial insight for the fourth Section (3.4), in which a new index, the Normalized Distance Red & SWIR (NDRS), was developed. In 3.1 and 3.2, the separability was compared for different seasons, addressing the question concerning the earliest date when it might be possible to differentiate between healthy and stressed pixels. Sections 3.3 and 3.4 focused more on estimating beetle attack precisely and efficiently.
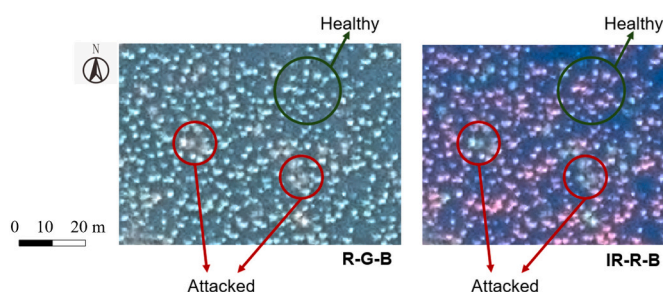
Fig. 3. Examples of attacked and healthy tree crowns in the Pleiades images.

3.1. Separability of individual bands

The backscatter σ^o from the VV (σ_{VV}) and VH (σ_{VH}) polarizations was extracted from the Sentinel-1 images for the healthy and attacked locations in Dataset-2018 (Fig. A1). The average σ_{VH} of the stressed pixels was higher than the healthy ones, and the difference was larger in the spring and autumn than in the summer. However, the difference between healthy and stressed pixels was still too small to identify stressed trees using only σ_{VV} or σ_{VH}.

The spectral values were extracted for the healthy and attacked locations from the Sentinel-2 images. In total we analyzed 10 bands and grouped them into visible (Bands 2, 3, 4), red-edge (Bands 5, 6, 7), NIR (Bands 8 and 8A), and SWIR (Bands 11 and 12) when presenting the results. The pixel values of healthy and stressed samples overlapped considerably in every band (Fig. A2).

Linear discriminant analysis (LDA) (Fisher, 1936) was conducted to quantify the separability of individual bands. This is a supervised classification using linear classifiers based on the distribution of features. The linear classifiers maximize the distance between classes and minimize the variance within classes. In the present study, LDA was conducted to each radar and optical band individually in each image. The leave-one-out cross-validation accuracy (overall classification accuracy, CA) was calculated to represent the linear separability of each band at the different stages of attack. A higher CA implies that the spectral band is more sensitive to the stress and hence has greater potential to identify stress successfully.

3.2. Classification using vegetation indices

In the present study, 12 spectral vegetation indices (Table 3) were computed and compared. The selected indices focused on the red band (Band 4), the NIR bands (Bands 8 and 8A) and the SWIR bands (Bands 11 and 12), which are sensitive to chlorophyll content, cell structure and vegetation moisture content, respectively. Of these, NDWI and RDI showed the largest difference between healthy and stressed pixels (Fig. A3), but they were still insufficiently separated for stress classification. Using the same analytical method as in Section 3.2, LDA was conducted with the vegetation indices, and the leave-one-out cross-validation accuracy was used to show how well the two classes were separated.

3.3. Combining multiple bands using a non-parametric method

The individual backscatter σ^o and spectral bands showed low separability of healthy and stressed pixels, as did classifications using existing vegetation indices. We therefore explored other alternative band combinations for stress identification. We used the Random Forest (RF) classification method to find additional combinations. The pixel values from all computed bands (radar and optical) were regarded as features in RF. Because the RF models set thresholds to features and give predictions based on these thresholds, all images were histogram-matched to the image of 6 July 2018 to avoid changes in pixel values from different seasons. An initial RF model was built using all bands (10 spectral bands, σ_{VH} and σ_{VV}) as features to show the relative importance of each band, which was presented by the Mean Decrease Accuracy (MDA) (Fig. A4). This is a measure of the decrease in the CA after changing a certain feature to random values. Higher MDA values therefore imply greater importance in the RF classification.

In the results section, the CAs are presented using RF models trained on Dataset-2018 and tested on Dataset-2019. Every training and testing was conducted using an individual image from different dates. Three RF models were built and tested for stress classification:

(1) Model A using Band 4 (red) and Band 12 (SWIR) as the features;
(2) Model B using Band 4 (red), Band 12 (SWIR) and σ_{VH} as the features;
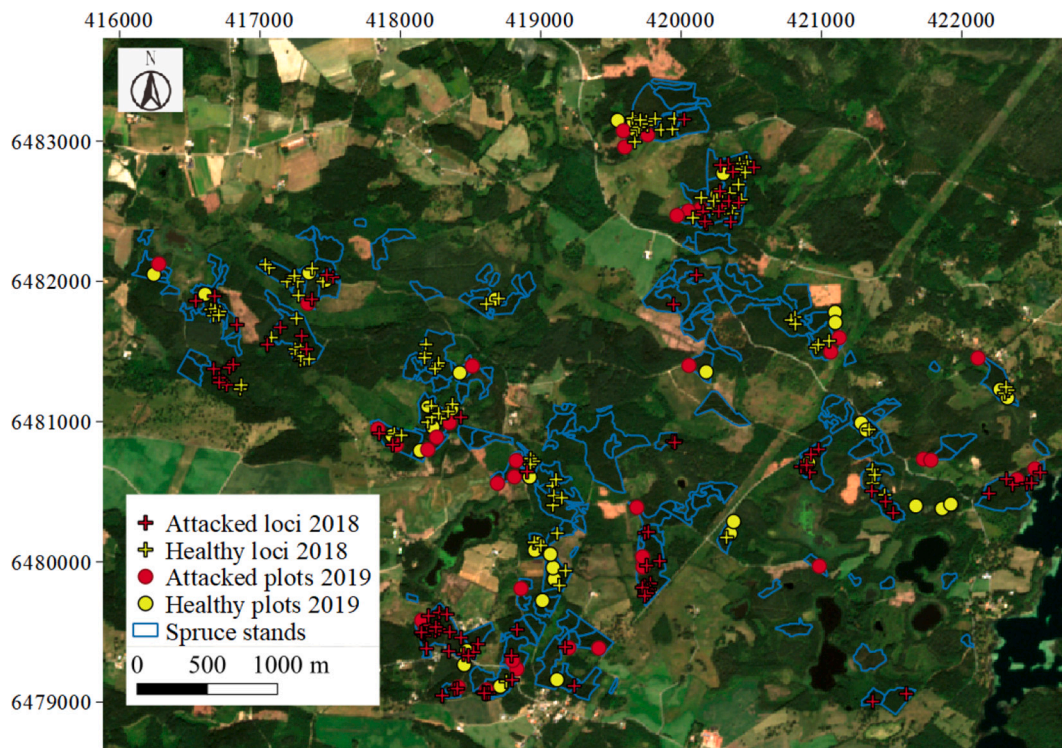
Fig. 4. The locations of Dataset-2018 and Dataset-2019. Background is the Sentinel-2 image with a true color composite from 6 July 2018.
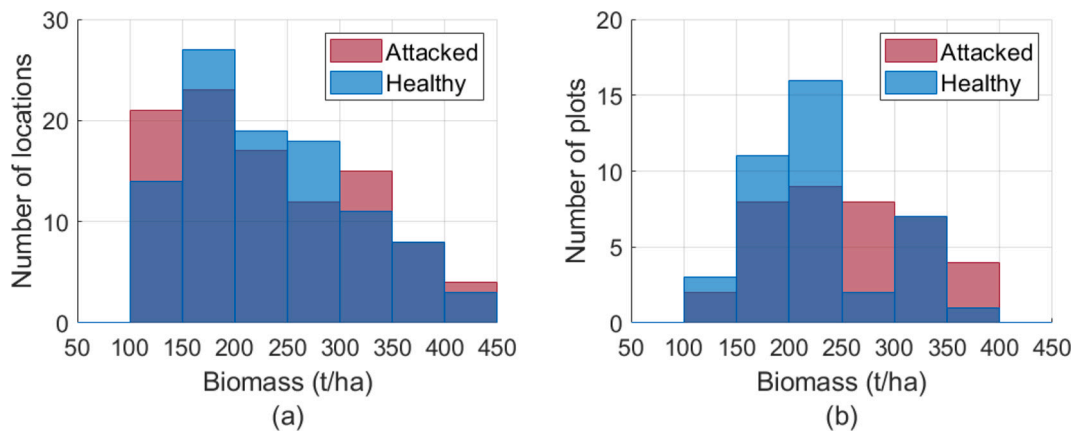
Fig. 5. Biomass distribution of Dataset-2018 (a) and Dataset-2019 (b).

(3) Model C using Band 4 (red), Band 12 (SWIR), σ_{VH} and σ_{VV} as the features.

These bands were selected based on the following criteria, as:

(1) Only one band from the SWIR bands was selected (Bands 11 and 12) because they are both sensitive to moisture and had a high correlation to each other (0.9942 in this study). Band 12 was selected because the CA decreased more than it did for Band 11 when removing them from the RF model. Based on a similar process, Band 4 was selected from the optical bands as one feature for the RF model.

(2) The results of adding backscatter σ^o were also presented, although they had lower importance than the optical bands when averaging the performance from different dates. The backscatter σ^o had low correlations with all optical bands, which means that they may contain additional information. Whether such

additional information would contribute to the classification was verified by observing the CA changes when adding them into the RF model with the selected optical bands.

The RF models were implemented using the 'randomForest' package (Liaw and Wiener, 2002) in R (R Core Team, 2019) with default parameter settings. The number of decision trees in the forest was 500. The number of features used as potential candidates for each split was $\sqrt{p}$ where p was the number of features. The minimum size of terminal nodes was one and with no maximum number of terminal node trees.

3.4. Definition of NDRS index

The analyses in Section 3.1 and 3.2 demonstrated that the existing vegetation indices separated the two classes insufficiently and that a combination of bands was needed for stress detection. A new index was therefore developed based on the optimized band combination derived
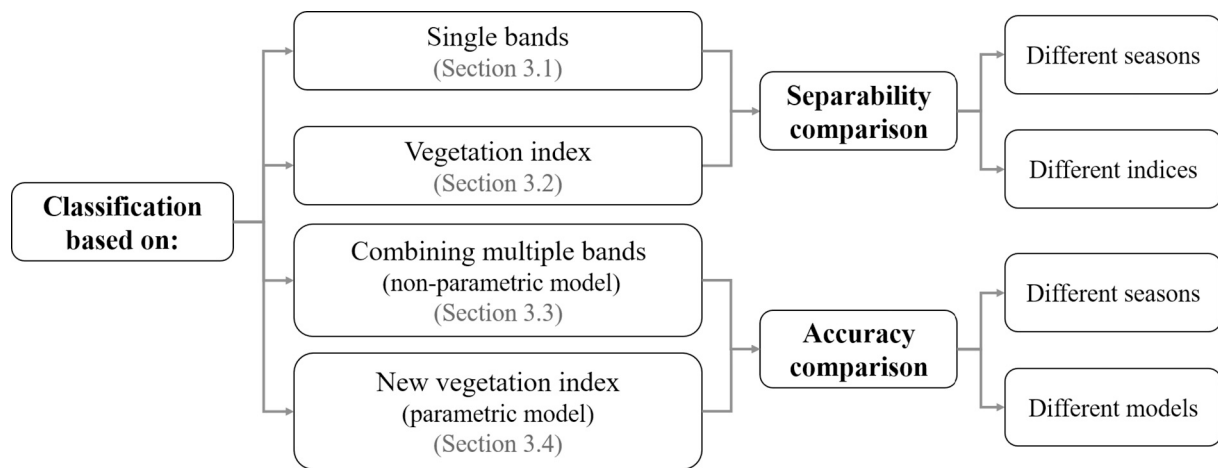
Fig. 6. Workflow of the study.

Table 3
Vegetation indices used in the present study.

No.	Abbr.	Name	Definition for Sentinel-2 bands (https://www.indexdatabase.de/)	Reference
1	NDWI	Normalized Difference Water Index	$\dfrac{Band\,8A - Band\,11}{Band\,8A + Band\,11}$	Gao (1996)
2	DSWI	Disease Stress Water Index	$\dfrac{Band\,8 + Band\,3}{Band\,4 + Band\,11}$	Galvão et al. (2005)
3	NGRDI	Normalized Green-Red Difference Index	$\dfrac{Band\,3 - Band\,4}{Band\,3 + Band\,4}$	Tucker (1979)
4	RDI	Ratio Drought Index	$\dfrac{Band\,12}{Band\,8A}$	Pinder and McLeod (1999)
5	GLI	Green Leaf Index	$\dfrac{(Band\,3 - Band\,4) + (Band\,3 - Band\,2)}{(Band\,3 + Band\,4) + (Band\,3 + Band\,2)}$	Louhaichi et al. (2001)
6	NDRE2	Normalized Difference Red-edge Index 2	$\dfrac{Band\,7 - Band\,5}{Band\,7 + Band\,5}$	Barnes et al. (2000)
7	PBI	Plant Biochemical Index	$\dfrac{Band\,8}{Band\,3}$	Abdullah et al. (2019c)
8	NDVI	Normalized Difference Vegetation Index	$\dfrac{Band\,8A - Band\,4}{Band\,8A + Band\,4}$	Rouse et al. (1973)
9	GNDVI	Green Normalized Difference Vegetation Index	$\dfrac{Band\,8A - Band\,3}{Band\,8A + Band\,3}$	Gitelson and Merzlyak (1998)
10	CIG	Chlorophyll Index Green	$\dfrac{Band\,8A}{Band\,3} - 1$	Gitelson et al. (2003)
11	CVI	Chlorophyll Vegetation Index	$\dfrac{Band\,8A \times Band\,5}{Band\,3 \times Band\,3}$	Hunt et al. (2011)
12	NDRE3	Normalized Difference Red-edge Index 3	$\dfrac{Band\,8A - Band\,7}{Band\,8A + Band\,7}$	Navarro et al. (2017)
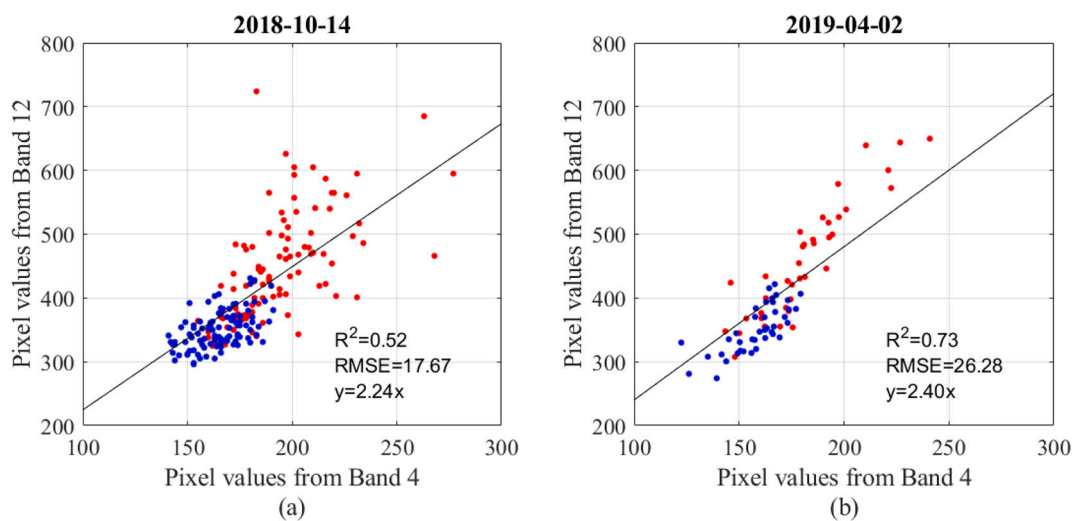
Fig. 7. Pixel values from Bands 4 and 12 in Sentinel-2 images. The pixel values are the bottom of atmosphere reflectance (12-bit, [0, 4095]). The pixels representing healthy (blue) and stressed (red) forest are shown for (a) the images of 14 October 2018, and (b) 2 April 2019. The solid black line is the regression line. (For interpretation of the references to color in this figure legend, the reader is referred to the web version of this article.)

from Section 3.3, i.e. Band 4 (red) and Band 12 (SWIR). These two bands had the greatest importance in the RF model, and there was a linear relationship between them (Fig. 7). This relationship was previously proposed by Kaufman et al. (1997), and has since been applied to an aerosol-free vegetation index. In our case, this relationship was observed both in Dataset-2018 and Dataset-2019, and the healthy and stressed pixel values were separated along the regression line (Fig. 7). The stressed pixels showed higher values in both the red and the SWIR bands, distributed further away from the origin. Based on this observation, the Distance Red SWIR, DRS, can be expressed as Eq. 1:

$$DRS = \sqrt{(Red)^2 + (SWIR)^2} \qquad (1)$$

To make the DRS sensitive to changes specifically appearing in spruce forest, the DRS was normalized to the range [0,1] for pixels representing spruce-dominated forest. This enabled us to provide a definition for the continuous distribution of attack probabilities; furthermore it allowed us to use fixed thresholds to classify the severity of stress in different seasons. The Normalized Distance Red SWIR (NDRS) was defined as Eq. 2.

$$NDRS = \frac{DRS - DRS'_{min}}{DRS'_{max} - DRS'_{min}} \qquad (2)$$

where DRS_{max}' and DRS_{min}' are the ranges of the DRS values for all spruce pixels in the image. By using values from individual images to perform the normalization, instead of a certain range based on all images, seasonal changes in the DRS could be eliminated. Thus, the threshold of NDRS for stress identification could be the same for all seasons. By using values based on spruce forest instead of the full image, the extremes from other land types, such as clear-cut areas, were removed. In the practical implementation, clear-cut patches often exist in the spruce stands due to sanitation. Normalization by the spruce pixels made the NDRS more sensitive to the subtle optical changes caused by the stress. In the present study, the 5% and 95% percentiles of the DRS values from all spruce stands were used as DRS_{min}' and DRS_{max}' to avoid any influence from extreme values that might be outliers. A similar principle of using the range of pixel values from the entire image when designing an index has been used for the Leaf Water Content Index (LWCI) (Hunt et al., 1987).

Two methods were used to classify the pixels into healthy and stressed classes. (1) A threshold of 0.5 was used to classify pixels as stressed if NDRS was higher than the threshold, or healthy if lower. This is intuitive and might be the simplest and most efficient method for practical implementation. The CA was compared with the results from Section 3.3, where a best-case scenario was evaluated. Both classifications used prior knowledge from the previous year and the evaluation accuracy on Dataset-2019 illustrated the implementation performance. (2) An LDA was used for classification from NDRS, and its accuracy was computed using leave-one-out cross-validation to show the performance. The CA represented the separability of NDRS between healthy and stressed pixels and could be compared with other vegetation indices used in Section 3.2. At the same time, this CA could illustrate the performance of NDRS when no reference data from previous years are available in the study area, but only reference data from the same year.

A small area (800 m × 900 m) was used as an example to demonstrate the mapping of estimated stress. The NDRS was calculated using images from different dates in 2018 and 2019. A set of thresholds defined as [0–0.4, 0.4–0.6, 0.6–0.8, 0.8–1.0] was used to classify pixels into healthy, low risk, moderate risk, and high risk. In this test area, some attacked trees were removed in the summer 2018, before the 2019 vegetation season. Therefore, the NDRS could also be used to identify pixels with clear-cuts, since they appeared as pixel values larger than 1. The changes between the maps from different dates represent how an NDRS could be used to map the spread of an infestation.

4. Results

4.1. Separability of individual bands

The radar signal showed slightly higher backscatter for stressed pixels than for the healthy ones (Fig. A1) especially in the spring and autumn. The spectral values from the stressed pixels showed a significant increase ($p < 0.05$ under Student's t-test) compared to the healthy ones throughout the whole vegetation season, including the period before attacks (Fig. A2).

Healthy and stressed pixels could not be sufficiently separated using only individual bands (Fig. 8). The CA was used to quantify the separability using LDA: a higher CA indicated a greater potential to distinguish stressed from healthy pixels. The separability of the individual bands could roughly be divided into three groups when considering the overall performance of all seasons:

(1) Bands 11 and 12 from the SWIR bands obtained higher CAs for healthy and stressed pixels than the visible, red-edge and NIR bands. Between these two SWIR bands, Band 12 obtained higher CAs than Band 11 before July, while the opposite was true after July.

(2) Bands 2, 3 and 4 from the visible band, and Band 5 from the red-edge bands obtained similar CAs and a similar changing trend among seasons. From June to October, the optical differences between the two classes became more and more significant. This is consistent with our visual experience, in that the stressed tree crowns exhibit gradual color changes from summer to autumn. Surprisingly, these bands showed even higher CAs in April and May than in June, especially Band 4, which had the highest CAs for most of the dates but the lowest CAs in the summer (June, July, and August).

(3) All the other optical bands and backscatter σ_{VH} and σ_{VH} exhibited similar CAs of around 0.6. Except for Band 8A and σ_{VH}, CAs for all the other bands in this group increased slightly and gradually with time. σ_{VV} obtained the lowest CAs among all bands, while σ_{VH} presented CAs similar to the NIR bands. Among the optical bands, the NIR bands exhibited the lowest separability. This implies that the NIR bands made only a limited contribution to the stress identification, at least in our dataset.

4.2. Classification using vegetation indices

The CAs for the existing vegetation indices (VIs) are presented in Fig. 9, using LDA. For comparison, the new NDRS index (Section 3.4) is also included, and will be further presented in Section 4.4. Most of the VIs exhibited stable separabilities before attacks, and the separabilities decreased during May or June, and gradually increased from June to August. When comparing April (before attacks) and August (end of 'green-attack'), the 'green-attack' symptoms resulted in insignificant increases in the separabilities, e.g. NDRS increased the CA from 0.83 to 0.84, RDI increased the CA from 0.72 to 0.78, and NDWI, only improved the CA from 0.75 to 0.77.

Among the commonly used VIs, the NDWI and RDI obtained the highest CA. Both of these indices used Band 8A and one of the SWIR bands. The DSWI index had the third highest CAs for most of the dates, which, in addition to the NIR and SWIR bands, also used Bands 3 and 4 from the visible bands. When comparing different VIs, we noticed that indices measuring water content generally appeared more sensitive to the bark beetle attacks than indices measuring chlorophyll. VIs with combinations of the NIR and SWIR bands generally had higher CAs than those with combinations of visible bands only, which in turn had higher CAs than those that combined NIR and visible bands. From the results in Section 4.1, the relatively lower CAs of the established VIs may be due to two reasons: (1) there is no VI that uses a combination of visible bands and SWIR bands; (2) many VIs contain the NIR bands which gave the
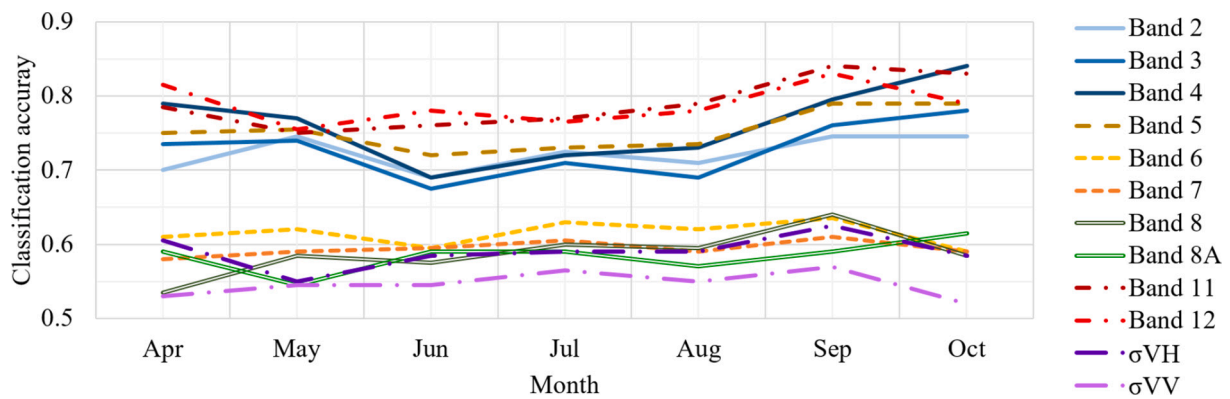
Fig. 8. Separability of individual bands shown by using CA from LDA and leave-one-out cross-validation.
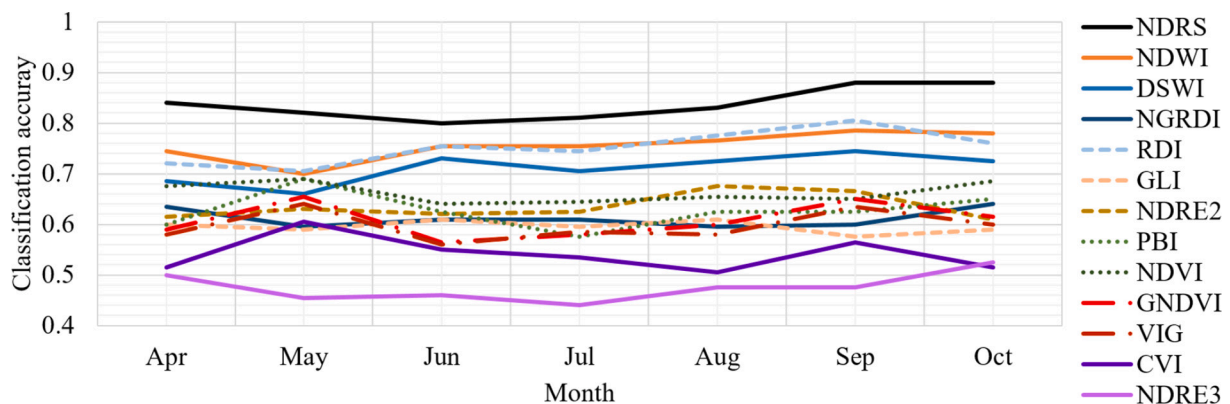
Fig. 9. Separability of vegetation indices for stress detection shown by CA from LDA and leave-one-out cross-validation.

lowest separability in this study.

4.3. Combining multiple bands using a non-parametric method

In this section, RF models were trained on seven individual images from 2018 using Dataset-2018, and each model was tested on six individual images from 2019 using Dataset-2019. The range of evaluated CAs for 2019 are presented as a boxplot (Fig. 10), with different training dates in 2018 used to identify whether images from any particular month were preferable to any other. The CAs varied between 0.7 and 0.85, but no clear trend could be seen during the season, except for the image from October where a tendency for a higher CA was noticed. This image was acquired after the growing season when the first frosts might occur. This was especially the case for model A (black bars) and C (red bars), while model B (blue bars) remained at the same level throughout the whole year.

Model C in particular showed a growing CA and increasing uncertainty from June to October. For the model using Band 4, Band 12, and σ_{VH} (abbr. Model B, blue bars in Fig. 10), there was no clear seasonal effect on the average CA. Each month gave similar levels of uncertainty except May when it was lower.

When considering the differences between these three models, Models A and C behaved similarly in terms of CA and uncertainty for most of the months, except Model C, which had a significantly higher CA

- CA of Model A, using Band 4 and Band 12.
- CA of Model B, using Band 4, Band 12, and σ_{VH}
- CA of Model C, using Band 4, Band 12, σ_{VH} and σ_{VV}
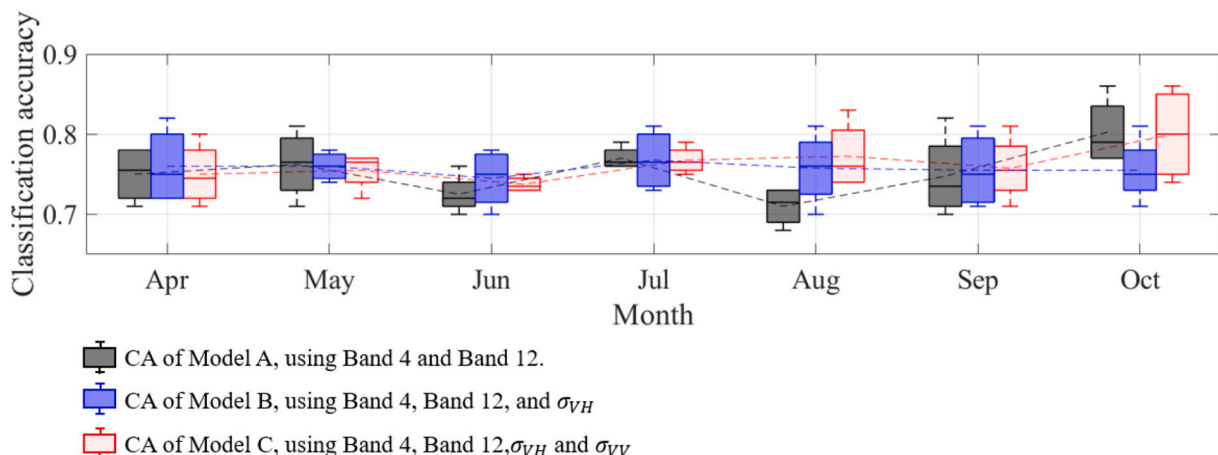
Fig. 10. CA displayed by the dates of training dataset of 2018 and tested on four images from spring 2019 based on the combination of the Sentinel-1 and 2 images.

in August and lower uncertainty in June. Compared to Models A and C, Model B exhibited the most stable performance over different months, while the other two exhibited more apparent differences in CA or uncertainty in certain months. Adding σ_{VH} to Bands 4 and 12 as features decreased the differences between months, and rendered the model more independent of the months selected for training.

4.4. NDRS index

The aim was that NDRS should separate the stressed samples from the healthy ones with higher accuracy than the existing VIs, especially from April to June, when early detection is required. To validate the performance of the NDRS, the index values were calculated for all images in 2018 and 2019. The separability of NDRS presented by the CA from LDA was included in Fig. 9. CAs from using NDRS increased by around 10% compared to CAs from using NDWI and RDI for all months.

The CAs from using NDRS decreased from April to June, and then increased in September. CA values in September and October were similar and obtained their highest values, while the lowest occurred in June. In April, which was before the attack, CA was similar to that of August. Fig. 11 shows the change of NDRS over time for the healthy and stressed samples. Both datasets showed increasing NDRS values for the stressed samples and stable values for the healthy ones. However, from April to July, the NDRS values for the stressed samples remained at the same level. These results imply that NDRS has the capacity to capture the forest stress before attacks, but is not sensitive to the changes caused by 'green-attacks', although detecting the stress contributed to the high accuracy for the detection of trees that were in the 'green-attack' stage.

The CAs when using 0.5 as the classification threshold are shown in Table 4 together with the CAs of other results in our study for comparison. The highest value of the CAs for 2018 was 0.89 in September and October, and the lowest value was 0.80 in June. The earliest available image in 2018 was from April, and its CA was 0.85. In 2019, four images were available in March and April, and their CAs ranged from 0.82 to 0.86. The implications of these results on our understanding of the early detection of bark beetle attack are discussed in Section 5.

Compared to LDA classification, using NDRS equal to 0.5 as the threshold caused over-fitting to Dataset-2018, which led to a higher CA for Dataset-2018 but a lower CA for the Dataset-2019. This result is consistent with the idea presented in Section 3.4. The CA from a fixed threshold should be compared with RF, because both are based on prior knowledge from the previous year and thus have a tendency to over-fit to the dataset in that year. Lower CAs would be obtained when validating the model on the predicted year using different samples. Our results show that NDRS has a more robust performance than RF in this aspect. The idea of setting the NDRS threshold for classification is suitable for the practical case when no reference data in the current year are available. This is also the only choice if an early detection map is required before the visible color changes in the infested tree crowns occur. Until the advanced infestation stage when the reference data can

be available for that year, the LDA would be a more generic method to implement over a large-area.

In addition to generating a static map of bark beetle attacks, the NDRS can also be used with time-series of satellite images to understand the pattern of spatial spread. In the appendices, we present a case study in order to demonstrate the implementation of NDRS to map the spreading pattern (Figs. A5 and A6). In this case study, an area with severe bark beetle attacks was selected. Fig. A5 shows the spatial spread of bark beetle infestations, with a large part of the maps consistent with the changes interpreted from the Pleiades images of 6 November 2018 and 17 July 2019 (Fig. A7). The maps in Fig. A5 describe the process of the infestation spreading from the forest edge into the interior.

5. Discussion

5.1. Characteristics of the stressed samples

This study has demonstrated the differences between healthy and stressed forest in time-series of radar and optical images. In the optical images, the stressed pixels showed higher average pixel values and higher variances than the healthy pixels in all bands. The increase of pixel values under stress was more prominent in the visible wavelengths (Bands 2, 3, 4) and the SWIR bands (Bands 11 and 12), while the red-edge wavelengths (Bands 5, 6, 7) and the NIR bands (Bands 8 and 8A) tended to show larger variations for the stressed pixels. This phenomenon was observed both before the first peak of swarming (middle April) and during May and June which were commonly considered as 'green-attacks'. Similar changes in the 'green-attacks' stage have been identified in other studies (Abdullah et al., 2019c; Klouček et al., 2019). Abdullah et al. (2018) observed a clear distinction of foliar chlorophyll, leaf water content and stomatal conductance between leaves from healthy and stressed trees. The reduction in chlorophyll decreases the spectral absorption in the visible region, resulting in relatively higher reflectance, especially in the red band (Carter and Knapp, 2001). During the attacks, as well as larval feeding causing phloem girdling (Wermelinger, 2004), beetle-associated blue-stain fungi may also dry the tissue and induce tracheid aspiration or vascular plugging (Paine et al., 1997). The changes of the water content caused by these processes could theoretically be observed with the SWIR bands (Gao, 1996).

Spectral differences between healthy and stressed samples existed at the beginning of the vegetation season before the attacks. During May and June, the differences did not increase significantly, which means the 'green-attack' had little influence on the spectral differences. Several bands and vegetation indices, such as NDRS, NDWI, DSWI, and RDI, showed even larger differences in April and May than in June. Similar results can also be seen in Fig. A2 of Abdullah et al. (2019c) using a dataset from Germany with RapidEye and SPOT-5 satellite images. When using multispectral UAV images, obvious differences in the red band were also observed on 4 April 2016 (Minařík and Langhammer, 2016). According to Lausch et al. (2013), obvious differences existed
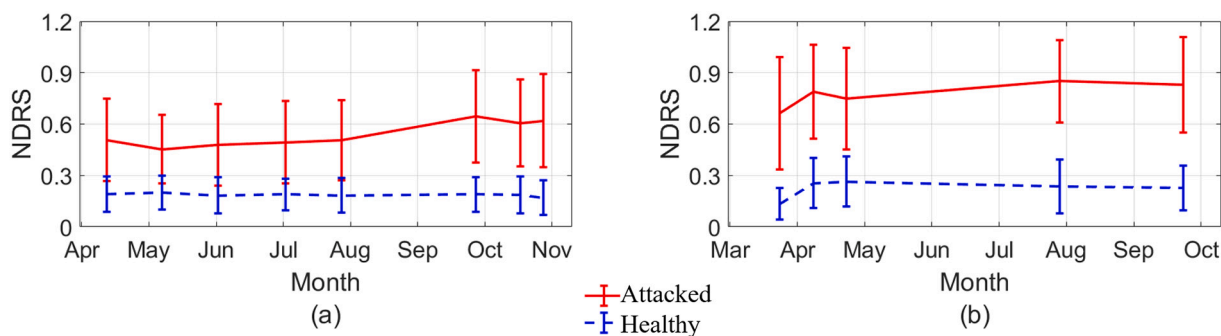
Fig. 11. The NDRS derived from different dates of 2018 (a) and 2019 (b) for healthy (blue) and stressed samples (red). (For interpretation of the references to color in this figure legend, the reader is referred to the web version of this article.)

Table 4

CA from RF model and 0.5 as the NDRS threshold. The accuracy on Dataset-2018 was training accuracy and Dataset-2019 was test accuracy.

Methods		Training accuracy							Evaluation accuracy					
	Features	Dataset-2018							Models trained on the image from October 2018 and tested on Dataset-2019					
		Apr	May	Jun	Jul	Aug	Sep	Oct	Mar	Apr	Apr	Apr	Jul	Sep
RF	Band 4, Band 12	0.80	0.72	0.73	0.73	0.78	0.82	0.84	0.81	0.77	0.86	0.77	0.76	0.81
	Band 4, Band 12, σ_{VH}	0.80	0.72	0.76	0.74	0.79	0.80	0.86	0.81	0.75	0.75	0.71	0.74	0.83
	Band 4, Band 12, σ_{VH}, σ_{VV}	0.80	0.74	0.75	0.74	0.77	0.80	0.85	0.86	0.76	0.84	0.74	0.76	0.81
NDRS	Using 0.5 as the threshold	Dataset-2018							Dataset-2019					
		Apr	May	Jun	Jul	Aug	Sep	Oct	Mar	Apr	Apr	Apr	Jul	Sep
		0.85	0.81	0.80	0.83	0.84	0.89	0.89	0.82	0.86	0.82	0.83	0.90	0.82
	Using LDA and leave-one-out cross validation	Dataset-2018							Dataset-2019					
		Apr	May	Jun	Jul	Aug	Sep	Oct	Mar	Apr	Apr	Apr	Jul	Sep
		0.84	0.82	0.80	0.81	0.83	0.88	0.88	0.85	0.88	0.86	0.83	0.91	0.86

even in previous years. They noted a higher reflectance for trees that were later attacked (in 2010 and 2011) already in the image from 25 August 2009. The higher reflectance was observed in all the measured bands with wavelengths between 450 nm – 2480 nm with a 4 m pixel size. Using images from 2009 contributed to predictions of the attacks in 2010 and 2011, with an accuracy of around 54% to 65%. These studies show that the spectral difference between healthy and attacked plots or trees are often present even before the attacks occur.

The spectral difference existing before attacks may be related to the weakness and stress, which induce the trees to be selected and later successfully infested by the bark beetles. In other words, the forest vulnerability was associated with spectral differences that contributed to the early estimation. At the individual tree level, bark anatomy and the physiological condition of a potential host tree are crucial for the success of a bark beetle attack (Wermelinger, 2004). At the stand level, factors influencing the attack probability include soil nutrients (such as nitrogen, phosphorus, and magnesium) (Dutilleul et al., 2000), water supply (Matthews et al., 2018; Netherer et al., 2019), the proportion of stand borders exposed to the south and west, the proportion of trees with heart rot, the age of the stand, the trend in radial growth, and the proportion of spruce (Wermelinger, 2004). Some of these factors have also been used in bark beetle attack prediction. For example, including topographic data, such as the calculation of wetness slope and brightness slope, significantly improved the predictive ability of bark beetle infestation models (Hais et al., 2016). In addition, one study found that the amount of weakened trees and sanitary felling because of abiotic factors in the previous year increased the probability of sanitary felling of Norway spruce because of bark beetles in the current year (de Groot and Ogris, 2019). These factors, by weakening and stressing trees, could be detected from satellite images as trends of spectral change even before attacks occurred.

5.2. Methods for stress detection

In this study, we developed a new vegetation index, NDRS, which was observed to have a stable performance in identifying stressed forest throughout the whole vegetation season. Using this index, the stress could potentially be detected early in the vegetation season, constituting an important part of an early warning system for forest management. Compared to other VIs, NDRS precisely highlighted the spectral difference between the healthy and stressed samples as early as April, May and June. Such early detection has been challenging for other VIs aiming at 'green-attack' detection.

We consider that the key reasons for the superior performance of NDRS compared to the other VIs are (1) the combination of the red and SWIR bands, and (2) avoiding using the red-edge and the NIR bands. Previous studies have reported different patterns of change in the red-edge and the NIR bands during bark beetle attacks. Although the two bands have been recommended for attack recognition due to the higher

reflectance averages in some studies (Abdullah et al., 2018; Minařík and Langhammer, 2016), others have stated such differences in reflectance to be insignificant (Klouček et al., 2019; Näsi et al., 2018). Therefore, the red-edge and the NIR bands may provide uncertain responses in identifying bark beetle stressed forest, and they should probably be cautiously implemented in practice. Factors that may cause the different responses included:

a. *Different responses for different pixel sizes.* Although significant decreases in the NIR bands have been observed for needles of attacked trees with a ground-based spectrometer, the same plots showed increased pixel values in the NIR band of RapidEye images and SPOT-5 images (Abdullah et al., 2019b). When attacked trees were observed from a UAV, the pixels returned lower average values than the healthy ones in images with 4 m resolution, but higher average values in images with 7 m resolution (Lausch et al., 2013). Such differences in response were also observed for the red-edge and NIR bands when comparing the six brightest pixels with all pixels of the crown (Näsi et al., 2015). It appears that the observed response in the NIR band is sensitive to the observation scale. With a larger pixel size or larger observation range in the tree crowns, the differences in reflectance in the NIR bands tends to weaken and disappear.

b. *Different responses to more specific wavelengths within the red-edge and NIR bands, respectively.* In WorldView-2 images, pixels of attacked trees had lower values than the healthy ones in the NIR band with wavelengths between 770 nm – 895 nm, but higher in the NIR band wavelengths of 860 nm – 1040 nm (Immitzer and Atzberger, 2014). In another study using Sentinel-2 images, pixel values from attacked trees showed significant decreases in Band 8 (833 nm central wavelength, 106 nm bandwidth), but insignificant changes in Band 8A (865 nm central wavelength, 21 nm bandwidth) (Abdullah et al., 2019b).

c. *Different responses to different sample properties,* e.g. *the proportion of attacked trees per observation unit, and the sample size.* Restricted by the infestation condition in our study area, the average proportion of attacked trees in the plots in 2019 was 30%, which was much lower than the 100% reported in the studies of Abdullah et al. (2019a, 2019b, 2019c). A mixture of healthy and attacked trees could weaken the spectral differences between healthy and attacked plots. Moreover, some studies have observed insignificant differences in the red-edge and NIR bands between healthy and attacked individual trees, although this may also be related to sample sizes being as small as ten (Klouček et al., 2019) or 15 (Näsi et al., 2015) attacked trees.

Compared to the unsystematic changes in the red-edge and NIR bands, many studies have reported significant increases in the SWIR bands from attacked trees (Fassnacht et al., 2014; Latifi et al., 2014; Lausch et al., 2013). Several studies have specifically pointed out the

importance of SWIR bands in detecting damage by bark beetles (Abdullah et al., 2018; Minařík and Langhammer, 2016). The separability analyses using LDA and feature importance analyses using RF in the present study confirm this conclusion. Furthermore, the new NDRS index, using the red and the SWIR bands, revealed more reliable and significant changes for attack estimation than the other 12 tested VIs using other bands. According to a review paper of different VIs (Xue and Su, 2017) and one online index database (https://www.indexdatabase.de/), indices using combinations of the red and the SWIR bands have rarely been used previously in any field. The new NDRS index was designed based on the linear relationship between the two bands. Such relationships were first proposed more than twenty years ago (Kaufman et al., 1997), and they have been used in an aerosol free vegetation index when replacing the red or the blue band by the SWIR band (1.6 and 2.1 μm) (Karnieli et al., 2001). The latter study included scatter plots of the relationship between the red and the SWIR bands from pixels covering different landscapes. The pixel values were distributed along the regression line, and additionally the pixels covering smaller proportions of forest were located further away from the origin. The index proposed in the present study extends the work from the previous studies, and furthermore, corroborates their findings.

When investigating the radar backscatter σ^o, the range of σ_{VH} increased slightly for the attacked trees. However, the difference was still insufficient to discriminate between healthy and attacked samples. Similar increases in the backscatter σ^o were observed in studies to detect bark beetle damage, when using images from the X-band with HH polarization, acquired with TerraSAR-X (Ortiz et al., 2013) and from the C-band with VH polarization when acquired with Sentinel-1 (Hollaus and Vreugdenhil, 2019). Furthermore, shoot beetle attacks showed an analogous pattern in Yunnan pine forest, when using Sentinel-1 images (Xue et al., 2018).

In our study, radar features were less important than spectral features when used in the RF classification. The contribution of radar data to attack detection has also been explored by Ortiz et al. (2013). Adding backscatter σ^o from TerraSAR-X images into a machine-learning model increased the accuracy compared to using spectral RapidEye images alone. It seems that radar data contain some useful information for identifying beetle attack, and that machine-learning methods are one way of extracting it. Bark beetle attacks are known to decrease the canopy water content (Abdullah et al., 2018), and attacks frequently happen to the locations with higher vegetation surface temperature. Bark beetle infestations often appear at the borders of forest stands, where exposure to the sunlight creates warmer conditions for the bark beetles to swarm. Mezei et al. (2019) identified beetle infestations more accurately when using solar radiation than other commonly used meteorological variables. Abdullah et al. (2019b) found an increasing canopy surface temperature in the attacked areas. Changes in the radar signal response may therefore be due to an interaction between the increasing temperature and decreasing moisture content (Hollaus and Vreugdenhil, 2019; Paloscia et al., 2013; Rüetschi et al., 2018; Way et al., 1990). Additional studies are required to test and verify this hypothesis.

When conducting infestation detection, we recommend studies to check the forest structure of the sampling data, considering that the forest structure is also a factor for the signal differences between the healthy and infested samples. In our study, the forest structure was controlled with a field inventory and using auxiliary data such as biomass maps, tree species maps and stand attribute tables. The plots in Dataset-2019 were subjectively selected such that the tree density and tree species composition were similar for all plots, in order to reduce effects due to the forest structure. For Dataset-2018, all locations were selected from stands older than 30 years and with spruce comprising more than 80% of the stem volume. The biomass was similarly distributed among healthy and attacked forest areas for both Dataset-2018 and Dataset-2019 (Fig. 2), which reduced the risk of mapping biomass rather than bark beetles. To ensure that the differences in radar and spectral

signals in our study were not due to biomass differences, we also conducted a linear discriminant analysis to identify attack using NDRS and biomass simultaneously. The results showed no discriminant line in the biomass dimension.

Since spectral differences between healthy and stressed trees could very well exist before the attacks, they should not necessarily be regarded as only a response to an infestation. Therefore, it is insufficient to conclude that 'green-attack' detection was achieved just by demonstrating spectral differences between the healthy and attacked samples. Although studies that have claimed to successfully detect a 'green-attack' have used field inventory data to prove that the attacked trees were indeed at the 'green-attack' stage, it does not follow that the spectral differences observed in the satellite images are actually caused by 'green-attack' symptoms. If the intention is to trace differences caused by 'green-attack' symptoms, we suggest that future studies should exclude the differences existing at the beginning of the attacks, and investigate the gradual changes of spectral reflection at the 'green-attack' and even later stages. However, if the intention is to identify stress early in the vegetation season - which is useful when instigating pest control procedures - the spectral difference could still be used to detect either stress before attacks or early-stage infestation using the methods proposed in the present study.

6. Conclusions

We investigated differences in radar and spectral signals between healthy trees and those attacked by spruce bark beetles. Signal differences between these two classes existed before attacks, and the differences did not increase during early-stage infestation, but only in autumn, the late-stage infestation. The differences in backscatter σ^o from Sentinel-1 images (C-band) were insufficient to estimate stress when used individually; neither did they contribute significantly to a non-parametric model when used together with spectral features. The red and SWIR bands exhibited the greatest potential for identifying stress among all the bands from Sentinel-2 images, while the NIR bands and Bands 6 and 7 from the red-edge bands showed the largest degree of overlap between the spectral values from healthy and attacked samples. These spectral differences contributed to the early warning of forest stress from bark beetle attacks, and thus could benefit the damage control and forest management.

A new index, NDRS, was proposed and validated for the estimation using the red and SWIR bands. The CA of the detection by NDRS in April (before attacks), June (early-stage infestation), and September (late-stage infestation) was 0.85, 0.80, and 0.89, respectively, for Dataset-2018. For Dataset-2019, images were only available before attacks and at the late stage, and CAs were 0.82–0.86 before attacks and 0.82–0.90 at the late stage. The CA was higher with NDRS than with NDWI and RDI, which were the VIs with the highest CA among those tested in the present study. These results demonstrated the feasibility of an early prediction of forest vulnerability to spruce beetle attacks with NDRS. NDRS could also be used to map and analyze the spatiotemporal spread of a spruce bark beetle infestation; this could be an important implementation of the method to further our understanding of factors affecting an infestation.

Declaration of Competing Interest

The authors declare that they have no known competing financial interests or personal relationships that could have appeared to influence the work reported in this paper.

Acknowledgements

Appendix A. Appendices
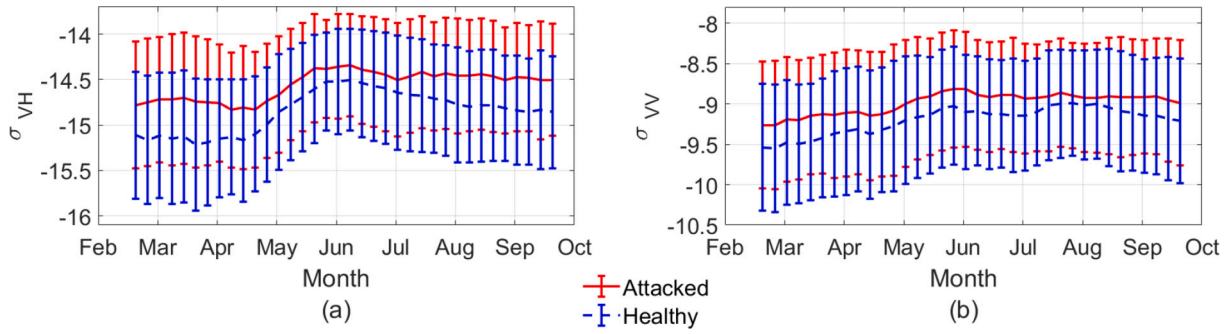
Fig. A1. σ_{VV} and σ_{VH} of healthy (blue) and attacked (red) pixels from the Sentinel-1 images using Dataset-2018.
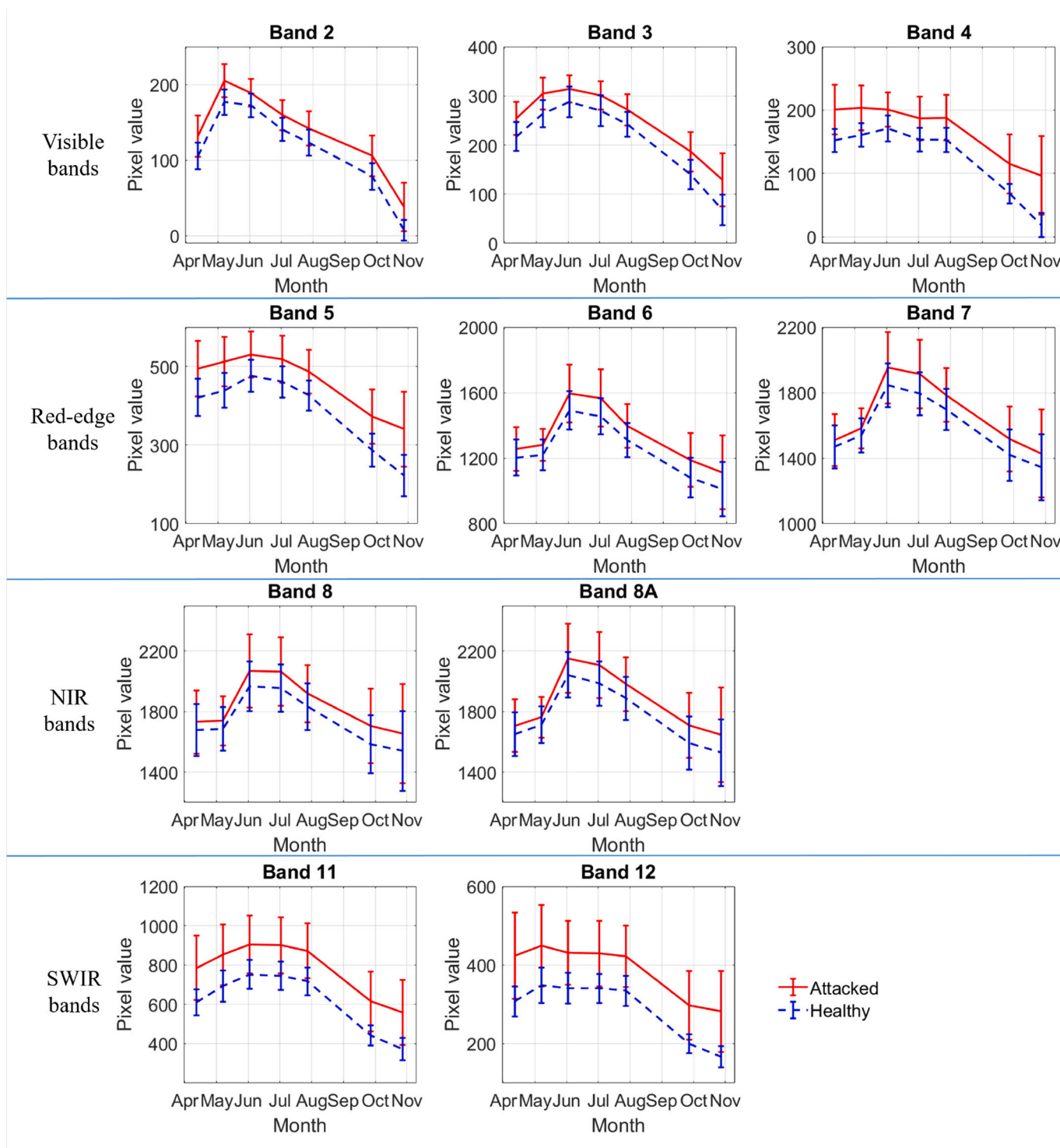
Fig. A2. The changes of pixel values in the time-series of Sentinel-2 images. The red and blue lines are the averaged pixel values of attacked and healthy pixels respectively, with standard deviation as the bar.
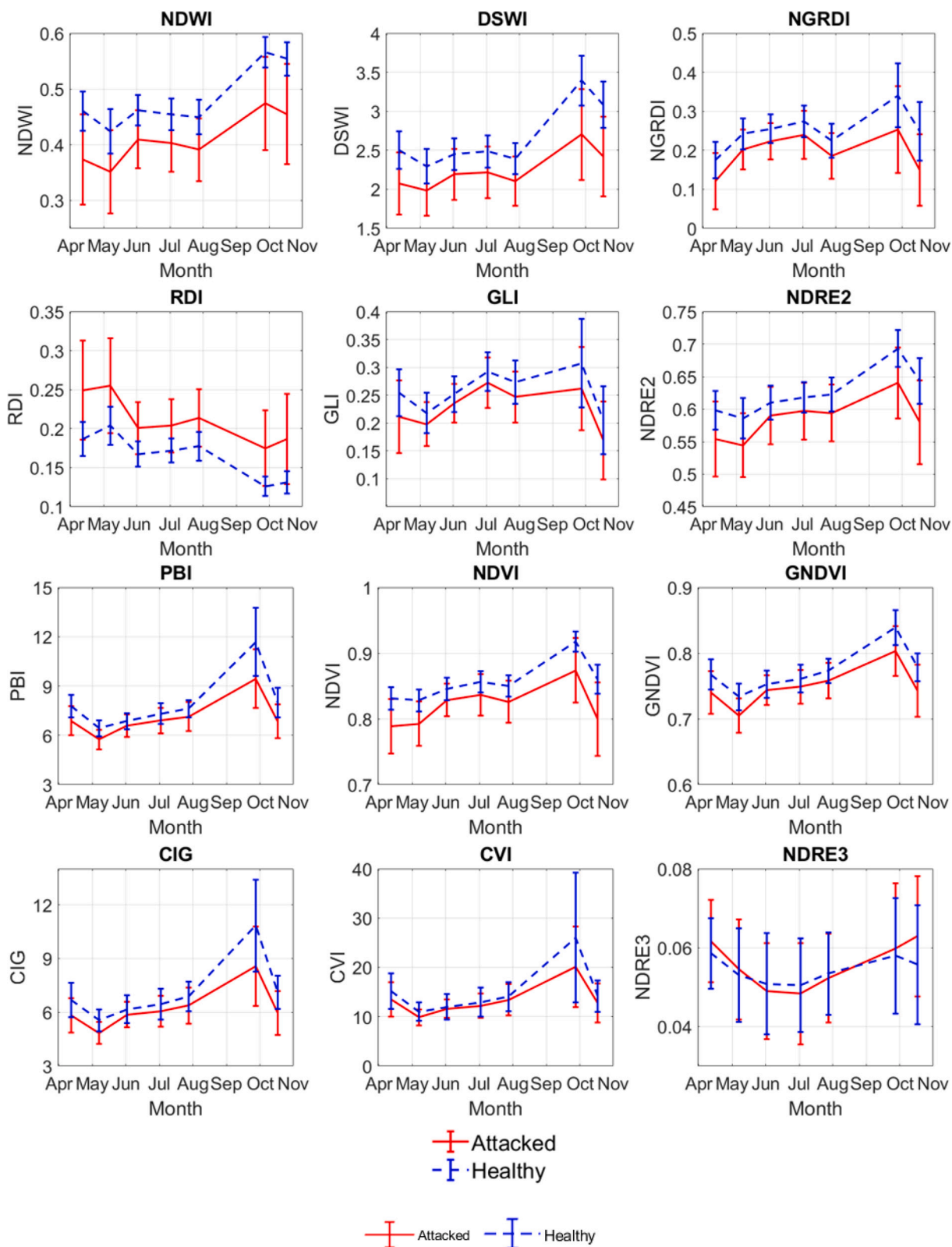
Fig. A3. Spectral vegetation indices for healthy and attacked pixels using the Sentinel-2 images. Red and blue lines are the averaged pixel values for attacked and healthy pixels respectively, with standard deviation as the bar.
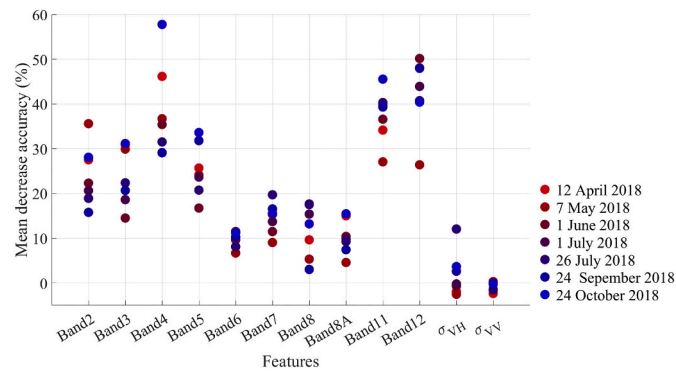
Fig. A4. MDA of each band from Sentinel-2 and σ_{VV} and σ_{VH} from Sentinel-1.
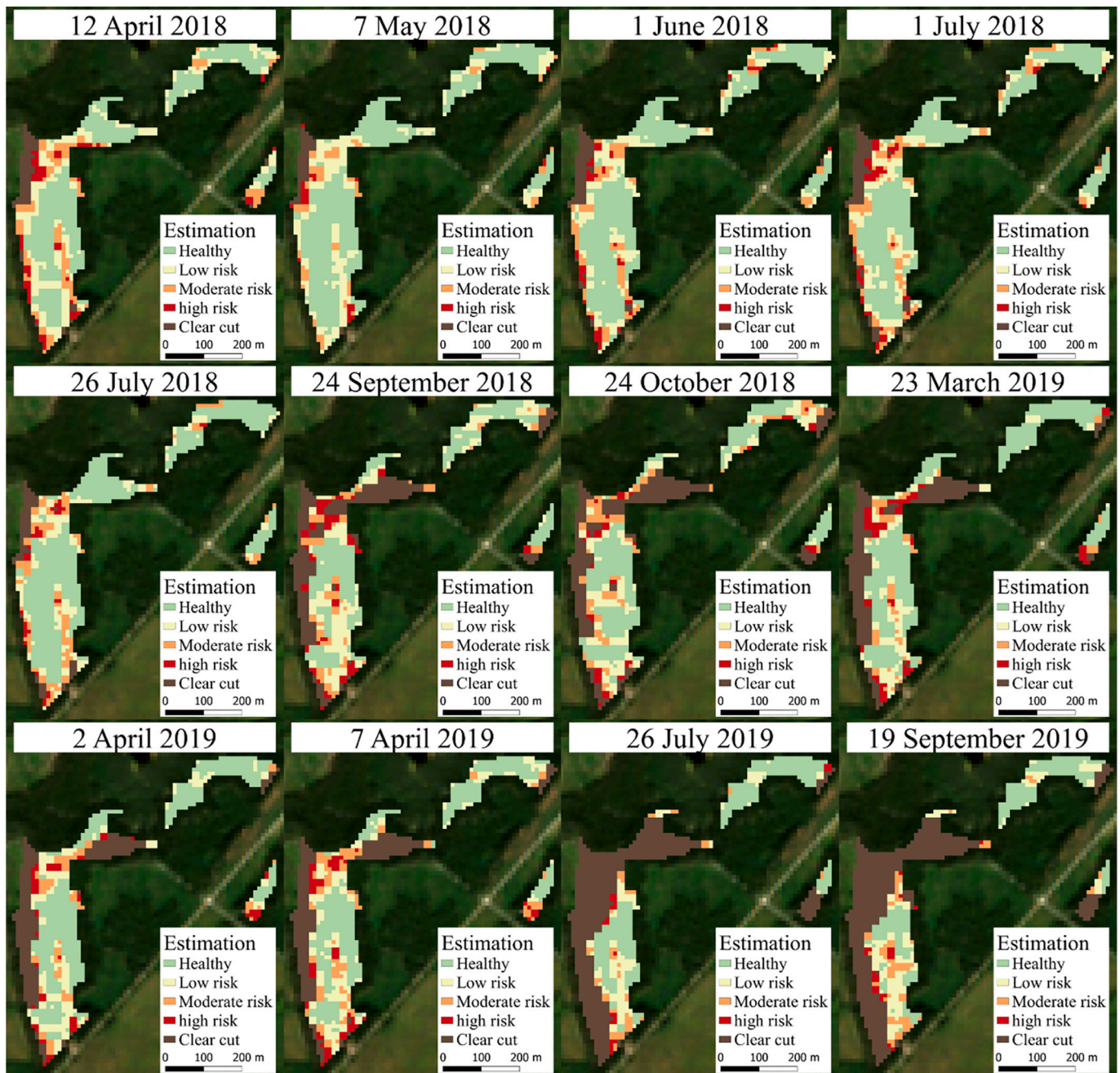
Fig. A5. A case study showing estimated attacks in a time-series and the spatial spread pattern of bark beetle infestations.
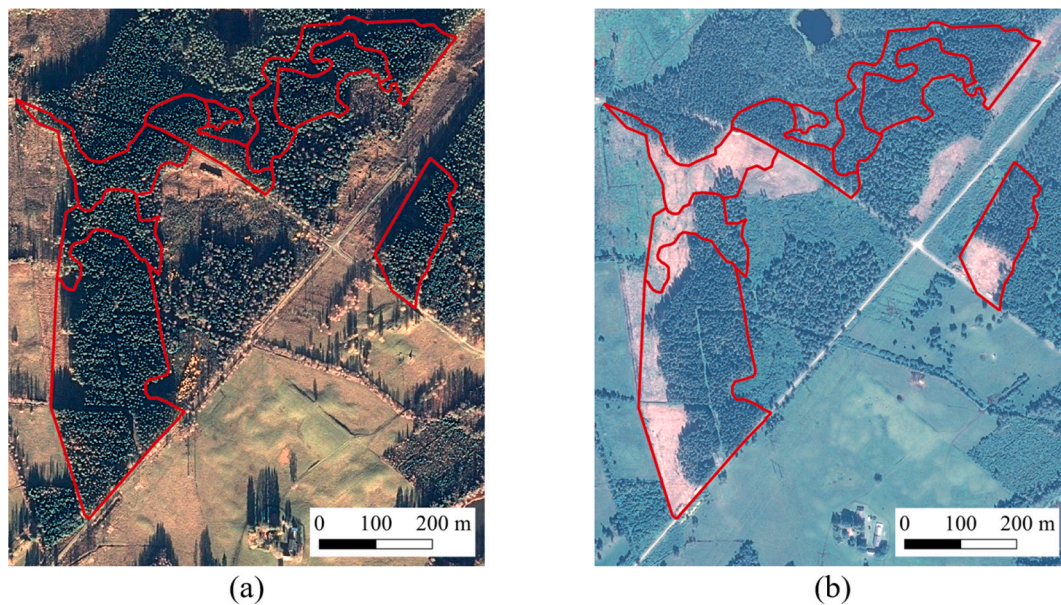
Fig. A6. The case study from Fig. A5 visualized with the Pleiades images from 6 November 2018 (a) and 17 July 2019 (b). In these stands, the clearing was only conducted for areas with serious infestations (provided by the local forest managers).

References

Abdullah, H.J., 2019. Remote Sensing of European Spruce (*Ips typographus*, L.) Bark Beetle Green Attack.

Abdullah, H., Darvishzadeh, R., Skidmore, A.K., Groen, T.A., Heurich, M., 2018. European spruce bark beetle (Ips typographus, L.) green attack affects foliar reflectance and biochemical properties. Int. J. Appl. Earth Obs. Geoinf. 64, 199–209.

Abdullah, H., Darvishzadeh, R., Skidmore, A., Heurich, M., 2019a. Sensitivity of Landsat-8 OLI and TIRS data to foliar properties of early stage bark beetle (*Ips typographus*, L.) infestation. Remote Sens. 11, 398.

Abdullah, H., Skidmore, A.K., Darvishzadeh, R., Heurich, M., 2019b. Sentinel-2 accurately maps green-attack stage of European spruce bark beetle (*Ips typographus* L.) compared with Landsat-8. Remote Sens. Ecol. Conserv. 5, 87–106.

Abdullah, H., Skidmore, A.K., Darvishzadeh, R., Heurich, M., 2019c. Timing of red-edge and shortwave infrared reflectance critical for early stress detection induced by bark beetle (*Ips typographus*, L.) attack. Int. J. Appl. Earth Obs. Geoinf. 82, 101900.

Barnes, E.M., Clarke, T.R., Richards, S.E., Colaizzi, P.D., Haberland, J., Kostrzewski, M., Waller, P., Choi, C., Riley, E., Thompson, T., Lascano, R.J., Li, H., Moran, M.S., 2000. Coincident Detection of Crop Water Stress, Nitrogen Status, and Canopy Density Using Ground-Based Multispectral Data.

Biedermann, P.H.W., Müller, J., Grégoire, J.-C., Gruppe, A., Hagge, J., Hammerbacher, A., Hofstetter, R.W., Kandasamy, D., Kolarik, M., Kostovcik, M., Krokene, P., Sallé, A., Six, D.L., Turrini, T., Vanderpool, D., Wingfield, M.J., Bässler, C., 2019. Bark beetle population dynamics in the anthropocene: challenges and solutions. Trends Ecol. Evol. 34, 914–924.

Carter, G.A., Knapp, A.K., 2001. Leaf optical properties in higher plants: linking spectral characteristics to stress and chlorophyll concentration. Am. J. Bot. 88, 677–684.

Chen, L., Wang, Y., Ren, C., Zhang, B., Wang, Z., 2019. Optimal combination of predictors and algorithms for Forest above-ground biomass mapping from sentinel and SRTM data. Remote Sens. 11, 414.

Coops, N.C., Johnson, M., Wulder, M.A., White, J.C., 2006a. Assessment of QuickBird high spatial resolution imagery to detect red attack damage due to mountain pine beetle infestation. Remote Sens. Environ. 103, 67–80.

Coops, N.C., Wulder, M.A., White, J.C., 2006b. Integrating remotely sensed and ancillary data sources to characterize a mountain pine beetle infestation. Remote Sens. Environ. 105, 83–97.

Coops, N.C., Varhola, A., Bater, C.W., Teti, P., Boon, S., Goodwin, N., Weiler, M., 2009. Assessing differences in tree and stand structure following beetle infestation using lidar data. Can. J. Remote. Sens. 35, 497–508.

R Core Team, 2019. R: A Language and Environment for Statistical Computing. Vienna, Austria. https://www.R-project.org/.

Dostálová, A., Wagner, W., Milenković, M., Hollaus, M., 2018. Annual seasonality in Sentinel-1 signal for forest mapping and forest type classification. Int. J. Remote Sens. 39, 7738–7760.

Dutilleul, P., Nef, L., Frigon, D., 2000. Assessment of site characteristics as predictors of the vulnerability of Norway spruce (Picea abies karst.) stands to attack by *Ips typographus* L. (Col., Scolytidae). J. Appl. Entomol. 124, 1–5.

Fassnacht, F.E., Latifi, H., Ghosh, A., Joshi, P.K., Koch, B., 2014. Assessing the potential of hyperspectral imagery to map bark beetle-induced tree mortality. Remote Sens. Environ. 140, 533–548.

Fisher, R.A., 1936. The use of multiple measurements in taxonomic problems. Ann. Eugenics 7, 179–188.

Foster, A.C., Walter, J.A., Shugart, H.H., Sibold, J., Negron, J., 2017. Spectral evidence of early-stage spruce beetle infestation in Engelmann spruce. For. Ecol. Manag. 384, 347–357.

Frison, P.-L., Fruneau, B., Kmiha, S., Soudani, K., Dufrêne, E., Le Toan, T., Koleck, T., Villard, L., Mougin, E., Rudant, J.-P., 2018. Potential of Sentinel-1 data for monitoring temperate mixed forest phenology. Remote Sens. 10, 2049.

Galvão, L.S., Formaggio, A.R., Tisot, D.A., 2005. Discrimination of sugarcane varieties in southeastern Brazil with EO-1 Hyperion data. Remote Sens. Environ. 94, 523–534.

Gao, B.-C., 1996. NDWI—A normalized difference water index for remote sensing of vegetation liquid water from space. Remote Sens. Environ. 58, 257–266.

Gitelson, A.A., Merzlyak, M.N., 1998. Remote sensing of chlorophyll concentration in higher plant leaves. Adv. Space Res. 22, 689–692.

Gitelson, A.A., Gritz, Y., Merzlyak, M.N., 2003. Relationships between leaf chlorophyll content and spectral reflectance and algorithms for non-destructive chlorophyll assessment in higher plant leaves. J. Plant Physiol. 160, 271–282.

de Groot, M., Ogris, N., 2019. Short-term forecasting of bark beetle outbreaks on two economically important conifer tree species. For. Ecol. Manag. 450, 117495.

Hais, M., Wild, J., Berec, L., Brůna, J., Kennedy, R., Braaten, J., Brož, Z., 2016. Landsat imagery spectral trajectories—important variables for spatially predicting the risks of bark beetle disturbance. Remote Sens. 8, 687.

Hollaus, M., Vreugdenhil, M., 2019. Radar satellite imagery for detecting bark beetle outbreaks in forests. Curr. Forest. Reports 60, 76.

Huang, C.-Y., Anderegg, W.R.L., Asner, G.P., 2019. Remote sensing of forest die-off in the anthropocene: from plant ecophysiology to canopy structure. Remote Sens. Environ. 231, 111233.

Hunt, R.E., Rock, B.N., Nobel, P.S., 1987. Measurement of leaf relative water content by infrared reflectance. Remote Sens. Environ. 22, 429–435.

Hunt, E.R., Daughtry, C.S.T., Eitel, J.U.H., Long, D.S., 2011. Remote sensing leaf chlorophyll content using a visible band index. Agron. J. 103, 1090–1099.

Immitzer, M., Atzberger, C., 2014. Early detection of bark beetle infestation in Norway spruce (*Picea abies*, L.) using WorldView-2 DataFrühzeitige Erkennung von Borkenkä ferbefall an Fichten mittels WorldView-2 Satellitendaten. Photogram. - Fernerkundung - Geoinform. 2014, 351–367.

Jakoby, O., Lischke, H., Wermelinger, B., 2019. Climate change alters elevational phenology patterns of the European spruce bark beetle (Ips typographus). Glob. Chang. Biol. 25, 4048–4063.

Junttila, S., Holopainen, M., Vastaranta, M., Lyytikäinen-Saarenmaa, P., Kaartinen, H., Hyyppä, J., Hyyppä, H., 2019. The potential of dual-wavelength terrestrial lidar in early detection of *Ips typographus* (L.) infestation – leaf water content as a proxy. Remote Sens. Environ. 231, 111–264.

Kaasalainen, S., Hyyppä, J., Karjalainen, M., Krooks, A., Lyytikäinen-Saarenmaa, P., Holopainen, M., Jaakkola, A., 2010. Comparison of Terrestrial Laser Scanner and Synthetic Aperture Radar Data in the Study of Forest Defoliation.

Kamińska, A., Lisiewicz, M., Stereńczak, K., Kraszewski, B., Sadkowski, R., 2018. Species-related single dead tree detection using multi-temporal ALS data and CIR imagery. Remote Sens. Environ. 219, 31–43.

Karnieli, A., Kaufman, Y.J., Remer, L., Wald, A., 2001. AFRI — aerosol free vegetation index. Remote Sens. Environ. 77, 10–21.

Kaufman, Y.J., Wald, A.E., Remer, L.A., Gao, B.-C., Li, R.-R., Flynn, L., 1997. The MODIS 2.1- µm channel—correlation with visible reflectance for use in remote sensing of aerosol. IEEE Trans. Geosci. Remote Sens. 35, 1286–1298.

Klouček, T., Komárek, J., Surový, P., Hrach, K., Janata, P., Vašíček, B., 2019. The use of UAV mounted sensors for precise detection of bark beetle infestation. Remote Sens. 11, 1561.

Latifi, H., Schumann, B., Kautz, M., Dech, S., 2014. Spatial characterization of bark beetle infestations by a multidate synergy of SPOT and Landsat imagery. Environ. Monit. Assess. 186, 441–456.

Lausch, A., Heurich, M., Gordalla, D., Dobner, H.-J., Gwillym-Margianto, S., Salbach, C., 2013. Forecasting potential bark beetle outbreaks based on spruce forest vitality using hyperspectral remote-sensing techniques at different scales. For. Ecol. Manag. 308, 76–89.

Liaw, A., Wiener, M., 2002. Classification and Regression by randomForest, 2. R News. https://CRAN.R-project.org/doc/Rnews/.

Louhaichi, M., Borman, M.M., Johnson, D.E., 2001. Spatially located platform and aerial photography for documentation of grazing impacts on wheat. Geocarto Intern. 16, 65–70.

Matthews, B., Netherer, S., Katzensteiner, K., Pennerstorfer, J., Blackwell, E., Henschke, P., Hietz, P., Rosner, S., Jansson, P.-E., Schume, H., Schopf, A., 2018. Transpiration deficits increase host susceptibility to bark beetle attack: experimental observations and practical outcomes for Ips typographus hazard assessment. Agric. For. Meteorol. 263, 69–89.

Meddens, A.J.H., Hicke, J.A., Vierling, L.A., 2011. Evaluating the potential of multispectral imagery to map multiple stages of tree mortality. Remote Sens. Environ. 115, 1632–1642.

Meddens, A.J.H., Hicke, J.A., Vierling, L.A., Hudak, A.T., 2013. Evaluating methods to detect bark beetle-caused tree mortality using single-date and multi-date Landsat imagery. Remote Sens. Environ. 132, 49–58.

Mezei, P., Potterf, M., Škvarenina, J., Rasmussen, J.G., Jakuš, R., 2019. Potential Solar Radiation as a Driver for Bark Beetle Infestation on a Landscape Scale. Forests 10 (7), 604.

Minařík, R., Langhammer, J., 2016. Use of a multispectral UAV photogrammetry for detection and tracking of forest disturbance dynamics. ISPRS - Intern. Archiv. Photogram. Remote Sens. Spatial Inform. Sci. XLI-B8, 711–718.

Näsi, R., Honkavaara, E., Lyytikäinen-Saarenmaa, P., Blomqvist, M., Litkey, P., Hakala, T., Viljanen, N., Kantola, T., Tanhuanpää, T., Holopainen, M., 2015. Using UAV-based photogrammetry and hyperspectral imaging for mapping bark beetle damage at tree-level. Remote Sens. 7, 15467–15493.

Näsi, R., Honkavaara, E., Blomqvist, M., Lyytikäinen-Saarenmaa, P., Hakala, T., Viljanen, N., Kantola, T., Holopainen, M., 2018. Remote sensing of bark beetle damage in urban forests at individual tree level using a novel hyperspectral camera from UAV and aircraft. Urban For. Urban Green. 30, 72–83.

Navarro, G., Caballero, I., Silva, G., Parra, P.-C., Vázquez, Á., Caldeira, R., 2017. Evaluation of forest fire on Madeira Island using sentinel-2A MSI imagery. Int. J. Appl. Earth Obs. Geoinf. 58, 97–106.

Navarro, J.A., Algeet, N., Fernández-Landa, A., Esteban, J., Rodríguez-Noriega, P., Guillén-Climent, M.L., 2019. Integration of UAV, Sentinel-1, and Sentinel-2 data for mangrove plantation aboveground biomass monitoring in Senegal. Remote Sens. 11, 77.

Netherer, S., Panassiti, B., Pennerstorfer, J., Matthews, B., 2019. Acute drought is an important driver of bark beetle infestation in Austrian Norway spruce stands. Front. Forest. Global Change 2, 265.

Ortiz, S., Breidenbach, J., Kändler, G., 2013. Early detection of bark beetle green attack using TerraSAR-X and RapidEye data. Remote Sens. 5, 1912–1931.

Paine, T.D., Raffa, K.F., Harrington, T.C., 1997. Interactions among Scolytid bark beetles, their associated fungi, and live host conifers. Annu. Rev. Entomol. 42, 179–206.

Paloscia, S., Pettinato, S., Santi, E., Notarnicola, C., Pasolli, L., Reppucci, A., 2013. Soil moisture mapping using Sentinel-1 images: algorithm and preliminary validation. Remote Sens. Environ. 134, 234–248.

Persson, H., Fransson, J., 2014. Forest variable estimation using Radargrammetric processing of TerraSAR-X images in boreal forests. Remote Sens. 6, 2084–2107.

Pinder, J.E., McLeod, K.W., 1999. Indications of Relative Drought Stress in Longleaf Pine From Thematic Mapper Data, 65, pp. 495–501.

Potterf, M., Nikolov, C., Kočická, E., Ferenčík, J., Mezei, P., Jakuš, R., 2019. Landscape-level spread of beetle infestations from windthrown- and beetle-killed trees in the non-intervention zone of the Tatra National Park, Slovakia (Central Europe). For. Ecol. Manag. 432, 489–500.

Puritch, G.S., 1981. Nonvisual Remote Sensing of Trees Affected by Stress–A Review: Environment Canada. Canadian Forestry Service, Pacific Forest Research Centre, Victoria, BC.

Ranson, K.J., Kovacs, K., Sun, G., Kharuk, V.I., 2003. Disturbance recognition in the boreal forest using radar and Landsat-7. Can. J. Remote. Sens. 29, 271–285.

Rouse, J., Haas, R., Schell, J., Deering, D., 1973. Monitoring Vegetation Systems in the Great Plains With ERTS.

Rüetschi, M., Schaepman, M.E., Small, D., 2018. Using multitemporal Sentinel-1 C-band backscatter to monitor phenology and classify deciduous and coniferous forests in northern Switzerland. Remote Sens. 10, 55.

Saatchi, S., Marlier, M., Chazdon, R.L., Clark, D.B., Russell, A.E., 2011. Impact of spatial variability of tropical forest structure on radar estimation of aboveground biomass. Remote Sens. Environ. 115, 2836–2849.

Schroeder, M., Cocoş, D., 2018. Performance of the tree-killing bark beetles Ips typographus and Pityogenes chalcographus in non-indigenous lodgepole pine and their historical host Norway spruce. Agric. For. Entomol. 20, 347–357.

Soja, M.J., Persson, H.J., Ulander, L.M.H., 2015. Estimation of Forest biomass from two-level model inversion of single-pass InSAR data. IEEE Trans. Geosci. Remote Sens. 53, 5083–5099.

Tanase, M.A., Aponte, C., Mermoz, S., Bouvet, A., Le Toan, T., Heurich, M., 2018. Detection of windthrows and insect outbreaks by L-band SAR: a case study in the Bavarian Forest National Park. Remote Sens. Environ. 209, 700–711.

Tane, Z., Roberts, D., Koltunov, A., Sweeney, S., Ramirez, C., 2018. A framework for detecting conifer mortality across an ecoregion using high spatial resolution spaceborne imaging spectroscopy. Remote Sens. Environ. 209, 195–210.

Tucker, C.J., 1979. Red and photographic infrared linear combinations for monitoring vegetation. Remote Sens. Environ. 8, 127–150.

Veloso, A., Mermoz, S., Bouvet, A., Le Toan, T., Planells, M., Dejoux, J.-F., Ceschia, E., 2017. Understanding the temporal behavior of crops using Sentinel-1 and Sentinel-2-like data for agricultural applications. Remote Sens. Environ. 199, 415–426.

Wang, Y., Day, J.L., Davis, F.W., 1998. Sensitivity of modeled C- and L-band radar backscatter to ground surface parameters in loblolly pine Forest. Remote Sens. Environ. 66, 331–342.

Way, J., Paris, J., Kasischke, E., Slaughter, C., Viereck, L., Christensen, N., Dobson, M.C., Ulayb, F., Richards, J., Milne, A., Sieber, A., Ahern, F.J., Simonett, D., Hoffer, R., Imhoff, M., Weber, J., 1990. The effect of changing environmental conditions on microwave signatures of forest ecosystems: preliminary results of the march 1988 Alaskan aircraft SAR experiment. Int. J. Remote Sens. 11, 1119–1144.

Wermelinger, B., 2004. Ecology and management of the spruce bark beetle Ips typographus—a review of recent research. For. Ecol. Manag. 202, 67–82.

White, J.C., Coops, N.C., Hilker, T., Wulder, M.A., Carroll, A.L., 2007. Detecting mountain pine beetle red attack damage with EO-1 Hyperion moisture indices. Int. J. Remote Sens. 28, 2111–2121.

Wulder, M.A., Dymond, C.C., White, J.C., Leckie, D.G., Carroll, A.L., 2006. Surveying mountain pine beetle damage of forests: a review of remote sensing opportunities. For. Ecol. Manag. 221, 27–41.

Wulder, M.A., White, J.C., Carroll, A.L., Coops, N.C., 2009. Challenges for the operational detection of mountain pine beetle green attack with remote sensing. For. Chron. 85, 32–38.

Xue, J., Su, B., 2017. Significant remote sensing vegetation indices: a review of developments and applications. J. Sens. 2017, 1–17.

Xue, J., Yu, L.F., Lin, Q.N., Guang, L., Huang, H.G., 2018. Using Sentinel-1 multi-temporal InSAR data to monitor the damage degree of shoot beetle in Yunnan pine forest. Remote Sens. Land Resourc. 30 (4), 108–114.

Yang, S., 2019. Detecting Bark Beetle Damage with Sentinel-2 Multi-Temporal Data in Sweden. Master, Sweden.